



OPEN

Frequency regulation in a hybrid renewable power grid: an effective strategy utilizing load frequency control and redox flow batteries

Ahmed H. A. Elkasem¹, Salah Kamel^{1✉}, Mohamed Khamies² & Loai Nasrat¹

Renewable energy sources (RESs) have become integral components of power grids, yet their integration presents challenges such as system inertia losses and mismatches between load demand and generation capacity. These issues jeopardize grid stability. To address this, an effective approach is proposed, combining enhanced load frequency control (LFC) (i.e., fuzzy PID- $T I^{\lambda} D^{\mu}$) with controlled energy storage systems, specifically controlled redox flow batteries (CRFBs), to mitigate uncertainties arising from RES integration. The optimization of this strategy's parameters is achieved using the crayfish optimization algorithm (COA), known for its global optimization capabilities and balance between exploration and exploitation. Performance evaluation against conventional controllers (PID, FO-PID, FO-(PD-PI)) confirms the superiority of the proposed approach in LFC. Extensive testing under various load disturbances, high renewables penetration, and communication delays ensures its effectiveness in minimizing disruptions. Validation using a standardized IEEE 39-bus system further demonstrates its efficiency in power networks grappling with significant renewables penetration. In summary, this integrated strategy presents a robust solution for modern power systems adapting to increasing renewable energy utilization.

Keywords Fuzzy-PID + ($T I^{\lambda} D^{\mu}$) controller, Crayfish optimization algorithm, Load frequency control, Renewable energy resources, Controlled redox flow batteries, Communication delay time

Abbreviations

RESSs	Renewable energy resources
PV	Photovoltaic
ESSs	Energy storage systems
SMES	Superconducting magnetic energy storage
SSSC	Static synchronous series compensator
PEVs	The plug-in electric vehicles
CRFBs	The controlled redox flow batteries
P.u	The value of the per unit
ACE	The area control error
U_{sh}	Undershoot
RLD	Random load disruption
O_{sh}	Overshoot
SLD	Step load disruption
AGC	The automatic generation control
MW	Mega-watt
LFC	Load frequency control
CDT	Communication delay time
FLC	Fuzzy logic control
T_{sim}	Total simulation time
dt	Error signal sampling interval

¹Department of Electrical Engineering, Faculty of Engineering, Aswan University, Aswan 81542, Egypt. ²Department of Electrical Engineering, Faculty of Engineering, Sohag University, Sohag 82524, Egypt. ✉email: skamel@aswu.edu.eg

TID	Tilted-integral-derivative controller
ISE	The integral square error
PID	Proportional-integral-derivative controller
ITAE	The integral time absolute error
FOCs	Fractional-order-controllers
FO-(PD-PI)	Fractional-order-proportional-derivative-proportional-integral controller
PD-PI	Proportional-derivative-proportional-integral controller
$TI^\lambda D^\mu$	Tilt-fractional-order-integral-fractional-order-derivative controller
FOPID	Fractional-order PID controller
HHO	Harris hawks optimization method
MRFO	Manta ray foraging optimization method
AOA	Arithmetic optimization algorithm
Min	Minutes
J	The objective function
Sec	Seconds
ESAOA	Eagle strategy arithmetic optimization algorithm
COA	Crayfish optimization algorithm
LMRFO	Leader manta ray foraging optimization
Δf_a	Area a frequency fluctuation
ΔP_{tiea-b}	Power flow from area-a to area-b via the tie-line
Δf_b	Area b frequency fluctuation
ΔP_{tieb-a}	Power flow from area-b to area-a via the tie-line
T_{ab}	Synchronization coefficient
a_{ab}	Capacity ratio of control area
K_T	The thermal unit's participation factor
B_a	Area a's frequency bias
K_G	The gas turbine's participation factor
B_b	Area b's frequency bias
K_H	The hydropower plant's participation factor
T_{cr}	Time delay regarding gas turbine combustion reaction
Y_c	Lag time constant regarding the speed governor of gas turbine
b_g	The gas turbine constant of valve positioner
c_g	The valve positioner of the gas turbine
\bar{T}_{cd}	Discharge volume-time constant regarding gas turbine compressor
T_{fc}	The fuel time constant of the gas turbine
\bar{X}_c	Lead time constant regarding the speed governor of gas turbine
T_r	The time constant of reheater steam turbine
T_t	The time constant of turbine
K_r	The gain of reheater steam turbine
R_1	The value of thermal turbine regulating constant
λ	The integrator's fractional-order
R_2	The value of hydropower plant regulating constant
μ	The differentiator's fractional-order
R_3	The value of gas turbine regulating constant
T_{sg}	The time constant of governor
P_{wt}	Generated wind turbine power
V_W	The speed of wind
C_p	The coefficient of rotor blades
ω_T	Speed of the rotor
A_T	A turbine's swept area
P	The density of air
r_T	The rotor radius
C_{1-C_7}	Turbine coefficients
B	The pitch angle
λ_i	The intermittent tip-speed ratio
λ_T	The optimum tip-speed ratio
T_{rs}	The speed governor reset time of the hydro turbine
T_{rh}	The transient droop time constant of the hydro turbine speed governor
T_{ps}	The time constant of power system
K_{ps}	The gain constant of power system
T_{gh}	The speed governor time constant of hydro turbine
T_w	The nominal string time of water in penstock

Background

Energy storage systems (ESSs) are becoming increasingly important as RESs become more prevalent in power systems. ESSs provide distinct benefits while also posing particular barriers in the field of energy storage, engaging a critical role in spanning the gap between energy generation and demand while integrating renewable

energy sources, but necessitating careful technological advances in selection, adaptability, and incorporation into existing infrastructure. On the other hand, it is essential to maintain equilibrium among power generation and demand in order to reinstate the power grid frequency to its desired orientation value. This task has been achieved by LFC¹. In recent times, the significance of LFC has grown substantially due to the expansion and complexity of interconnected power grids, rising operational costs, and the limitations of traditional units. These factors can potentially result in inadequate control performance. To address these challenges, extensive research has been conducted considering LFC, with a particular revolve around exploring the potential benefits of demand response. Numerous studies in the literature have aimed to investigate and comprehend how demand response², ESSs^{3–5}, RESs for example photovoltaic (PV) plants⁶, flexible alternative current transmission system controllers⁷, and wind turbine generators⁸.

State-of-the-art literature review

The traditional approach to frequency control in power grids involves approximating the system as a linear model based on a specific operating condition without taking into account the dynamics of the generators. One commonly used method for frequency regulation is proportional-integral-derivative (PID) control, which has been commonly applied in the ancient due to its merits such as affordability and simplicity. Nevertheless, PID controllers are susceptible to vagaries in system constraints (e.g., system uncertainty and nonlinearities)⁹. However, in recent years, several control strategies, such as fractional order controllers (FOCs)^{10,11}, fuzzy logic control (FLC)¹², sliding mode control¹³, artificial neural network¹⁴, and model predictive control (MPC)¹⁵, has been developed to address the frequency deviation problem.

In contrast, FOCs offer numerous advantages for power system stabilization, providing a boarder extent of freedom and increased configuration flexibility. These characteristics make FOCs a perfect option for controlling power grids. Unlike traditional PID controllers, FOCs require the fine-tuning of different types of poles, like hyper-damped poles, which expands the stable area and provides increased design flexibility for controllers. As a result, FOCs reduce overshoot, the settling time, as well as undershoot values, surpassing PID controllers and their variations. Furthermore, wide-ranging researches have been conducted on the tender of FOCs in various studies, with two common forms being firstly, the title integral derivative (TID) form as well as the fractional order PID (FOPID)⁴. These FOCs have been thoroughly researched with the goal in order to boost the stability of frequency of today's electrical power grids^{16–18}. While these controllers have demonstrated promising results in normal operating conditions.

In addition, the fuzzy controller offers several key benefits, including its straightforward implementation, its ability to effectively respond to system variations, as well as its ability to accommodate variations in the operational situations or system constraints through online updates of the controller constraints. These advantages stem from the controller's simplicity in execution and its high sensitivity to fluctuations in the power grid¹⁹. The initial application of FLC in addressing the LFC problem involved combining it with a PID controller, as described in²⁰. Furthermore, a self-tuning fuzzy-PID controller has been introduced to improve the stability of the frequency of a two-area power grid²¹. Moreover, the fuzzy-PID controller has been employed to stabilize the power structure's frequency that incorporates multiple power sources²². According to the merits of FOCs and FLC, the authors proposed the (fuzzy-PID) + (T I^λ D^μ) controller to handle the LFC problematic in the analyzed two-area interconnected power grid. However, the FLC utilizes various strictures such as inputs, scaling factors, membership functions, and rule base. But, there are no fixed rules to determine the values of these parameters. Typically, trial-and-error methods have been employed to choice these values, but they may not always yield optimal performance. To address this issue, a meta-heuristic technique known as the Crayfish Optimization Algorithm (COA) has been used to select the optimal constraints of the proposed controller.

Lastly, multiple controllers in the LFC issue have been addressed through the application of optimization methods including a tracking methodology²³ and aggregation strategies²⁴ have been used to address. However, these prior techniques have certain downsides. To address the limitations of traditional optimization methods, which can get trapped in local minimums, require a high number of iterations, and are sensitive to initial conditions, researchers have focused their attention on meta-heuristic optimization methods, for example Coyote Optimization Algorithm²⁵, Dandelion Optimizer²⁶, Harris Hawks Algorithm²⁷, Archimedes Optimization Algorithm²⁸, Sine Cosine Algorithm²⁹, Ant Colony Optimization³⁰, Whale Optimization Algorithm³¹, Grey Wolf Optimizer³², Artificial Bee Colony Algorithm³³, Imperialist competitive Algorithm (ICA)³⁴, Quasi-oppositional Harmony Search^{35,36}, Quasi-opposition Pathfinder Algorithm³⁷, Chaotic Chimp Sine Cosine Optimization Algorithm³⁸, Quasi-oppositional Whale Optimization Algorithm³⁹. These alternative approaches have gained attention as they offer a way to overcome these limitations and find optimal solutions more efficiently. By leveraging meta-heuristic optimization techniques, researchers can enhance the performance of LFC controllers and find more robust and effective parameter settings. Accordingly, the authors propose applying the COA algorithm to determine the finest constraints of the considered controller. As, the considered COA method has been developed to address the limitations associated with traditional optimization techniques. The COA method offers advantages over conventional optimization algorithms by employing a gradient-free mechanism, which helps overcome the issue of getting stuck in local solutions. Moreover, the COA algorithm has the capability to find global solutions using a small number of search agents, further enhancing its superiority over other optimization methods⁴⁰. In this work, it is the first time to apply the COA technique in handling the LFC issue.

From a different perspective, when there is a large impact as well as a high penetration of renewable energy, the frequency and tie line may be different for a long time, and oscillations may still occur. In this case, the LFC response may not be sufficient to absorb the frequency change due to the slowness and poor quality of the response. As a result, it is necessary to apply ESSs. However, different studies have applied different energy storage

strategies with rapid rejoinder, like superconducting magnetic energy storage (SMES), fuel cell systems (FCSs), plug-in electric vehicles (PEVs), and redox flow batteries (RFBs), for addressing the LFC issue. The utilization of these devices has emerged as a new and intriguing research area^{3,4,41–47}. Among these, RFB has shown its advantages over other electronic devices (such as SMES) due to its ability to operate at normal temperature, low loss and long service life. Consequently, RFBs is anticipated to be the most effective solution⁴⁸. In a study described in⁴⁹, the influence of RFBs and SMES units on enhancing the performance of a power grid was investigated. Simulation outcomes indicated that the incorporation of RFB units more effectively dampened dynamic responses in comparison to the SMES units. Additionally, the authors of demonstrated the superior performance of RFBs in combination with the Unified Power Flow Controller and Interline Power Flow Controller in Automatic Generation Control (AGC) on nonlinear power systems^{43,50}. Furthermore, the stability is achieved in a nonlinear power system by incorporating integral control of the LFC model with RFBs storage and a Static Synchronous Series Compensator⁵¹.

Research gap

Despite the pre-mentioned studies successfully achieved their objectives, these studies did not focus on the high incorporation of RESs in the presence of high load demand. For example, more than one previous study focused on conventional power plants and did not adequately consider the impact of RESs^{7,22,41,42}. Nevertheless, the present study emphasizes high renewables penetration like wind and solar energy, which are commonly utilized in both areas of the power grid under examination. Additionally, numerous studies overlook the influence of diverse load perturbation shapes, which can be essential for evaluating the applied controller^{25,26,28,30,31}. However, this study considered numerous load perturbation profiles like, step load disruptions (SLD), series SLD, and random load disruptions (RLD) which represent the forced outage of power plants or high change on the load demand. Moreover, most previous studies considered applying different types of ESSs without applying any controller to control their output^{5,43}. However, this study consider the controlled ESSs to control the amount of the power which will injected to the overall system. The standard IEEE 39 buses test system is considered. Furthermore, the durability of the indicated controller is examined in this work by considering the challenge of the communication delay time (CDT). The purpose is to validate the effectiveness of the proposed controller in achieving stability and reliability in a practical power system setting. Furthermore, this paper's main objective is to address the limitations uncovered in previously published investigations concerning the frequency stability problem. Therefore, Table 1 provides a clear overview of the variances between this study and other researches in the literature, emphasizing the unique contributions and approaches taken in this paper.

Article motivations and contributions

The scope and contribution of this research can be summarized as follows:

- Proposing a concerted strategy based on enhanced LFC in coordination with ESSs (i.e., CRFBs) improves power grid stability during periods of disturbances in load and high RESs penetration. Where the proposed controller in LFC is (fuzzy-PID) + (T I^λD^μ) controller, whose superiority is confirmed by comparing its performance with other controllers like the (PID, FO-PID, PD-PI and FO-(PD-PI)).
- Considering the COA technique to select the optimal parameters of the considered controllers, according to its good optimization properties (i.e., balancing between exploration and exploitation) in order to enhance the performance of the analyzed power grid.
- The superiority of the proposed strategy is validated considering high RESs, load disturbances as well as CDT in considered hybrid power grid. Furthermore, the standard IEEE 39 buses is considered to confirm the superiority of the proposed strategy.

References	5	7	16	22	49	51	This work
Controller design	Combining TD-TI	Fuzzy fine-tuning approach	Cascaded TID	Fuzzy logic based self-tuning PID	PI	I	(fuzzy-PID) + (T I ^λ D ^μ)
High penetration levels of RESs	√	×	×	×	×	×	√
Additional improvements incorporation	Considered PEVs	Considered series capacitors	Considered capacitor	not considered	Considered RFBs/ SMES	Considered RFBs/ SSSC	Considered CRFBs
Real-time validation considering various load patterns	×	×	×	×	×	×	IEEE-39 bus system/ SLD
Real-time validation considering high RESs penetration	×	×	×	×	×	×	√
Real-time validation considering CDT	×	×	×	×	×	×	√

Table 1. Comparison of the present work's motivation to those of other published studies.

The remaining content of the manuscript is structured as follows: "Background" provides a detailed overview of the power grid under investigation, emphasizing its substantial penetration of renewable energy sources and the integration of controlled redox flow battery (CRFB) systems within the proposed strategy. "State-of-the-art literature review" describes the recommended approach, which involves the fuzzy-PID and $(T I^{\lambda} D^{\mu})$ controller, and formulates the problem under analysis. "Research gap" outlines the methodology employed for the crayfish optimization algorithm (COA) procedure. "Article motivations and contributions" presents the simulation results obtained from the aforementioned scenarios. Finally, in "Modeling of an investigated system", the study's conclusions and key findings are discussed and reviewed.

Modeling of an investigated system The configuration of the considered system base

The power grid that is mentioned in the literature is a two-identical area, with a three-traditional unit included within each area. A tie-line connecting the two areas is an AC tie-line. Thermal, hydro, and gas turbines are the three conventional units, which are dispersed throughout the two zones. In the present study, a 2000 MW, total capacity electrical system is examined. In contrast, having a 1087 MW, contribution, the thermal unit has the biggest capacity. The second-largest capacity, contributing 653 MW, is possessed by the hydropower facility. And finally, 262 MW, is contributed by the gas turbine capacity. Furthermore, Fig. 1 simplifies the diagram of the examined power grid, while the block diagram of the examined power grid is illustrated as Fig. 2. Next, each block's mathematical equation from Fig. 2 is presented in detail in Table 2. For the purpose of dealing with fluctuations in frequency in each area (e.g., area a -area b) and control the tie-line power flow between them, a (fuzzy-PID) + $(T I^{\lambda} D^{\mu})$ controller is proposed to be implemented for each power plant. The Area Control Error (ACE) serves as the input signal for the controller, while the output signal represents the specific supplementary control action for each power plant. The aim of this procedure is to produce additional active power in order to improve the currently assessed grid performance. Appendix A provides comprehensive information about all the parameters related to the analyzed power grid, including their nominal values⁵². The following equations describe the formularies used to calculate the ACEs related to interconnected areas.

$$ACE_a = \Delta P_{tiea-b} + B_a \Delta f_a \tag{1}$$

$$ACE_b = \Delta P_{tieb-a} + B_b \Delta f_b \tag{2}$$

Conceptualization of the wind farm

As highlighted in this analysis, the study's power grid is a hybrid system that contains a significant proportion of RESs, with a focus on wind generating facilities. The following formulae can be used to calculate wind output power^{3,4}.

$$P_{wt} = \frac{1}{2} \rho A_T v_w^3 C_p(\lambda, \beta) \tag{3}$$

The wind output power, denoted as P_{wt} (in MW), is determined by various factors. These factors include the flounced sectioned area, A_T (in m^2), the tip-speed ratio (TSR), λ , the power coefficient, C_p , of the rotor blades,

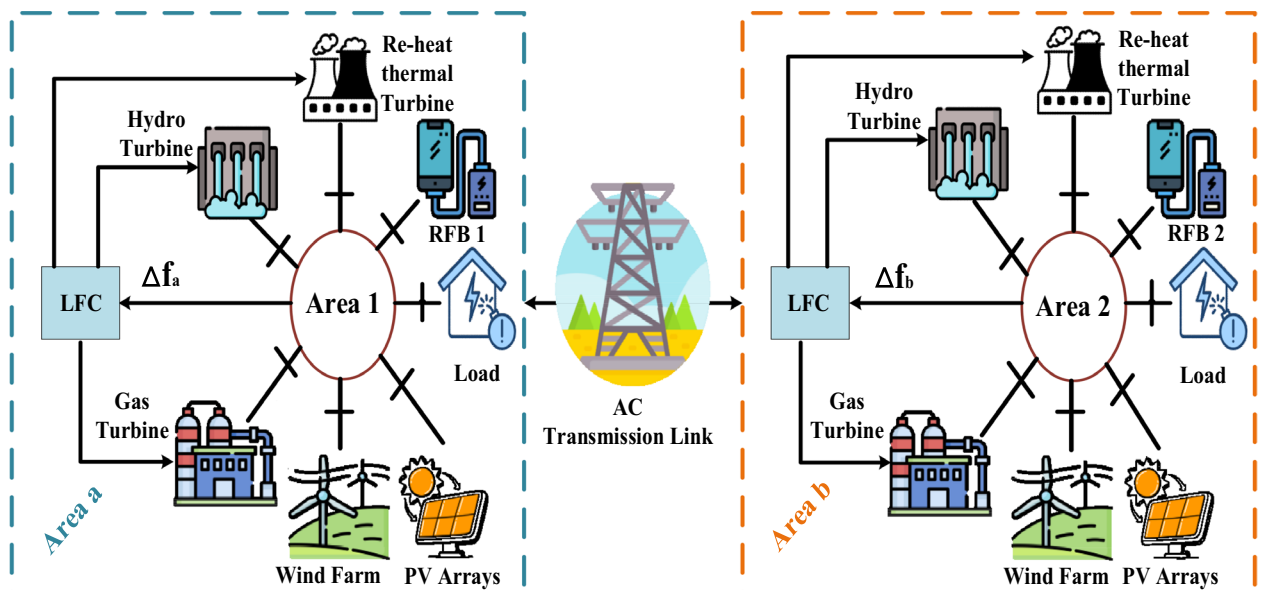


Figure 1. Schematic diagram of the considered grid.

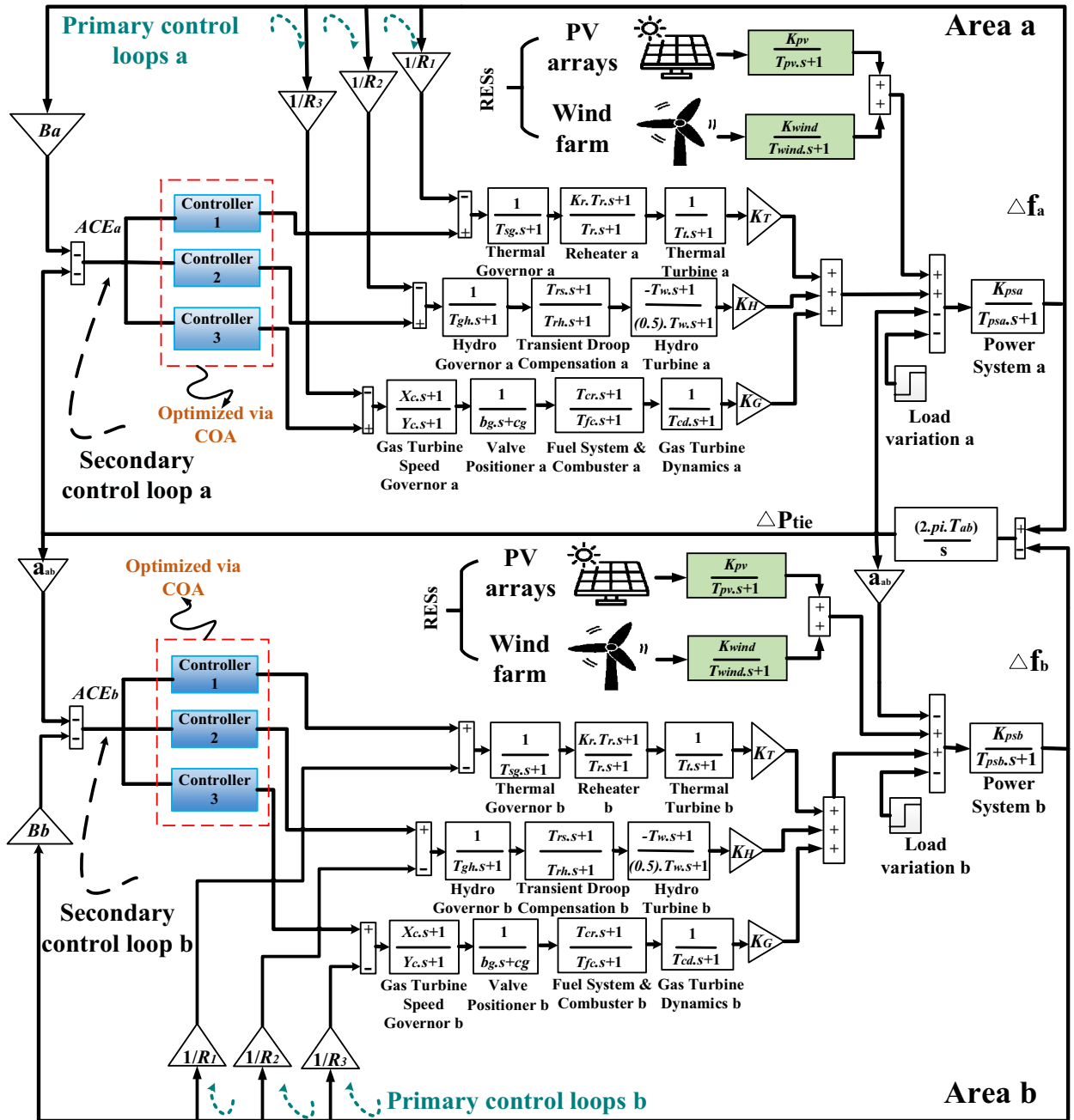


Figure 2. The linearized model of the Power grid under investigation.

the air density, ρ (in kg/m^3), the wind speed, V_w (in m/s), and the blade pitch angle, β . The C_p can be expressed as follow⁵³:

$$C_p(\lambda_i, \beta) = 0.5(\lambda_i - 0.022\beta^2 - 5.6) \times e^{-0.17\lambda_i} \tag{4}$$

$$\lambda_i = \frac{3600 \times R}{1609 \times \lambda} \tag{5}$$

$$\lambda = \frac{\omega_B \times R}{V_w} \tag{6}$$

where ω_B specifies the angular velocity value of the blade (rad/sec).

The wind farm at Zafarana, Egypt, with a total installed capacity of 85 MW, is included in this study. Additionally, Fig. 3 presents the real output power data for the Zafarana windmill. One may theoretically describe

Description of A block	Formulation of transfer functions
Power system a	$\frac{K_{psa}}{T_{psa} \cdot s + 1}$
Power system b	$\frac{K_{psb}}{T_{psb} \cdot s + 1}$
Hydro turbine	$\frac{-T_w \cdot s + 1}{(0.5) \cdot T_w \cdot s + 1}$
Transient droop compensation	$\frac{T_{td} \cdot s + 1}{T_{td} \cdot s + 1}$
Hydro governor	$\frac{1}{T_{gh} \cdot s + 1}$
Reheater of thermal turbine	$\frac{K_r \cdot T_r \cdot s + 1}{T_r \cdot s + 1}$
Thermal governor	$\frac{1}{T_{sg} \cdot s + 1}$
Thermal turbine	$\frac{1}{T_t \cdot s + 1}$
Gas turbine's speed governor	$\frac{x_c \cdot s + 1}{y_c \cdot s + 1}$
Gas turbine dynamics	$\frac{1}{T_{td} \cdot s + 1}$
Gas turbine's valve positioner	$\frac{1}{b_g \cdot s + c_g}$
Fuel system and combustor	$\frac{T_{fc} \cdot s + 1}{T_{fc} \cdot s + 1}$
Synchronizing coefficient	$\frac{(2 \cdot \pi \cdot T_{ab})}{s}$
Wind farm	$\frac{K_{wind}}{T_{wind} \cdot s + 1}$
PV Power plant	$\frac{K_{pv}}{T_{pv} \cdot s + 1}$

Table 2. The mathematical formulas regarding the considered power grid blocks.

the characteristics of the transfer function, which depicts the behavior of the integrated induction generator in a wind power plant, as 0.3 s for the time constant (T_{wind}) and a unity gain (K_{wind}). Additionally, the overall capacity applied in this work is ten Zafarana wind farms, with a total capacity of 850 MW.

Conceptualization of the photovoltaic (PV) power plant

This research also takes into account photovoltaic (PV) power plants, which generate electricity from solar energy besides utilized wind farms. Multiple variables, like the PV cell's surface area, the intensity of solar radiation, and the surrounding air temperature, affect a PV system's output power. For calculating the amount of energy generated by the module of PV in this current study, an equation is employed, taking into account these factors.

$$P = \eta_{sc} \tau_g \alpha_{sc} RA [1 - \mu_{sc} (T_{sc} - T_r)] \tag{7}$$

In the PV system, several parameters influence the output power calculation. These parameters include the cell reference efficiency denoted as η_{sc} , the entire solar cell's (SC) surface area denoted as A (measured in m^2), the solar radiation denoted as R (measured in W/m^2), the transmissivity of the glass denoted as τ_g , the absorptivity of the SC denoted as α_{sc} , the PV cell efficiency thermal coefficient denoted as μ_{sc} (measured in $\frac{\%}{^\circ C}$), the temperature of the SC denoted as T_{sc} (measured in $^\circ C$), then the reference temperature signified as T_r (measured in $^\circ C$). These parameters are used in a formula to determine the PV module's electrical power output.

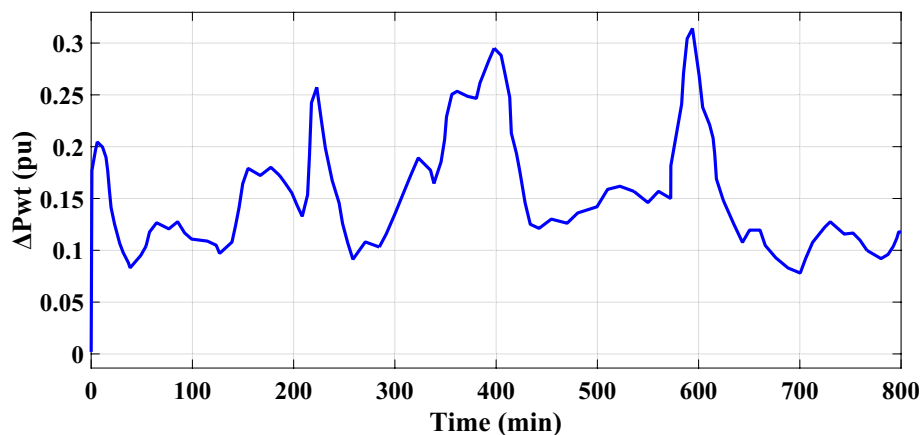


Figure 3. Energy generated by the Zafarana windmill station⁵³.

This study focuses on a specific power grid and examines a realistic 50 MW PV system. The southern Egypt represents the location of this aforementioned realistic PV power plant. Whereas, the realistic PV power plant is modeled by a transfer function with 10 ms time constant (T_{PV}) and a unity gain (K_{PV}). The output power of this PV system is depicted in Fig. 4 illustrates the diagram of the output power produced by the PV system. Appendix B provides the results of the analysis of data gathered for identifying the correlation between brightness and PV temperature. Furthermore, the characteristics of the studied PV system are displayed in Figs. 5,6, which emphasize the associations between the produced active power, the values of brightness, the produced active power, and the temperature of the surroundings. Additionally, the overall capacity applied in this work is ten realistic PV power plants, with a total capacity of 500 MW.

Controlled redox flow batteries (CRFBs) conceptualization

The CRFBs functions as an electrochemical power source that has the ability to be recharged. CRFBs can rapidly and efficiently save energy for the power network; additionally it can also employ the generator's kinetic energy when requested⁵⁰. It functions as a rapid energy compensating equipment for high load electrical consumption and additionally aids in frequency fluctuation suppression. The CRFBs has a broad range of applications and

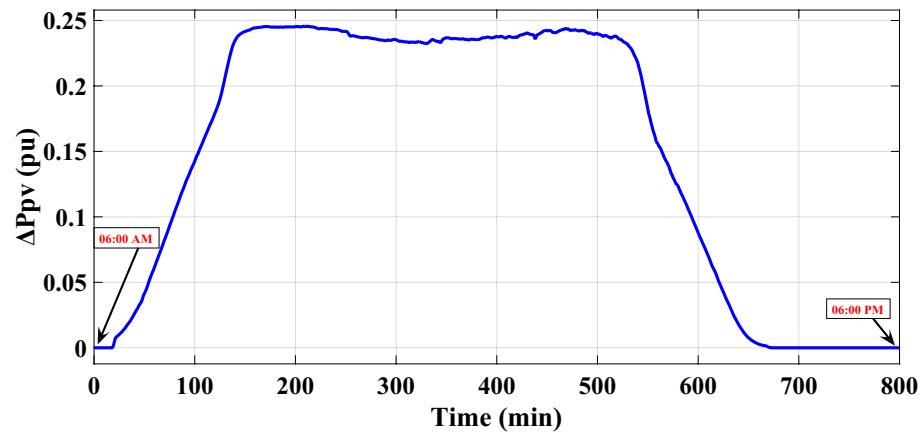


Figure 4. The exact PV power plant power generation⁵³.

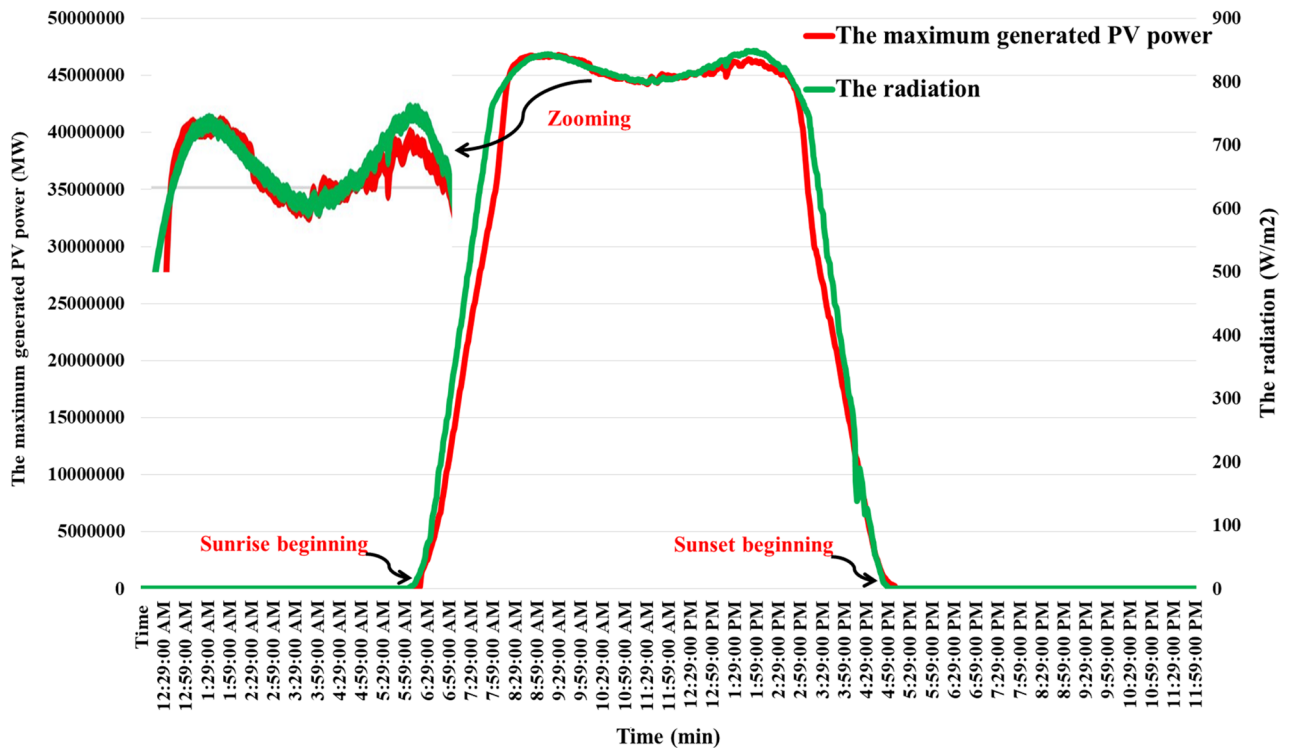


Figure 5. Radiation and power generation characteristics of the PV energy station.

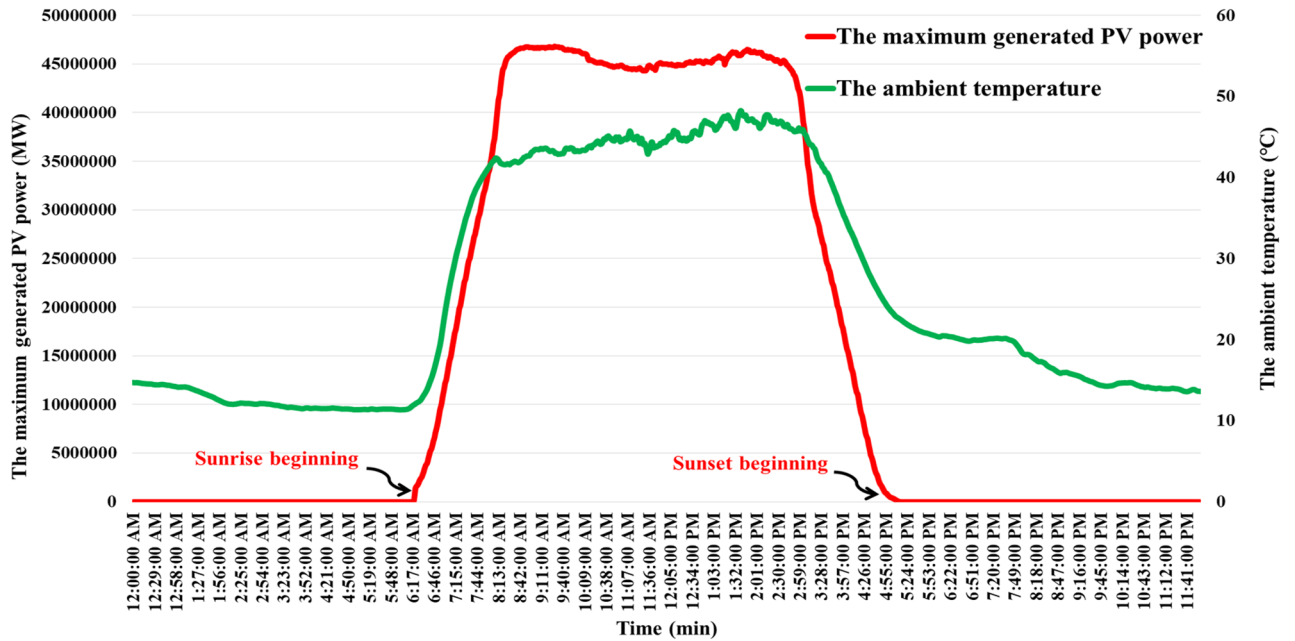


Figure 6. Power generation characteristics and ambient temperature of the PV energy station.

offers excellent features such as improved power quality, load compensation, higher capacity compared to conventional batteries, quick response time, and independence from self-discharge issues. During low load demand periods, the CRFBs stores and saves the energy that is equivalent to the demand variations. This stored energy can then be unrestricted back into the grid during load fluctuations, aiding in the elimination of power grid oscillations.

In this study, a significant aspect of CRFBs modeling is the utilization of a comprehensive and realistic dynamic model of redox flow batteries, rather than the simplistic first-order transfer function models commonly used in several recent papers. The model incorporates the Δf (change in frequency) as an input. This paper presents a controller design that incorporates a feedback path to generate control signals for CRFBs. This design enables the CRFBs to respond efficiently to disturbances, resulting in improved performance. The designed controller, denoted as $K(s)$, is considered as a PID controller in this work. The relevant parameters of the CRFBs are provided in the Appendix B. Figure 7 illustrates the block diagram of CRFBs. Equation (8) indicates how the CRFBs unit is woven into the studied power grid⁴⁵.

$$\Delta P_{CRFBi} = \left[k_{p,CRFBi} \Delta f_i \times \left(\frac{1 + s}{1 + k_{r,CRFBi} + s(T_{r,CRFBi} + T_{d,CRFBi}) + s^2 T_{r,CRFBi} T_{d,CRFBi}} \right) - initial\ value \right] \times K(s) \tag{8}$$

Proposed control mechanism and problem description

In order to address the difficulties caused by the high renewables penetration, several load profile themes, and communication delays, it is crucial to design a reliable controller that can boost system performance under irregular situations. This paper recommends the utilizing of a (fuzzy-PID) + $(T I^{\lambda} D^{\mu})$ controller to alleviate the deviations resulting from the aforementioned factors. Structure-wise, both the TID and PID controllers are

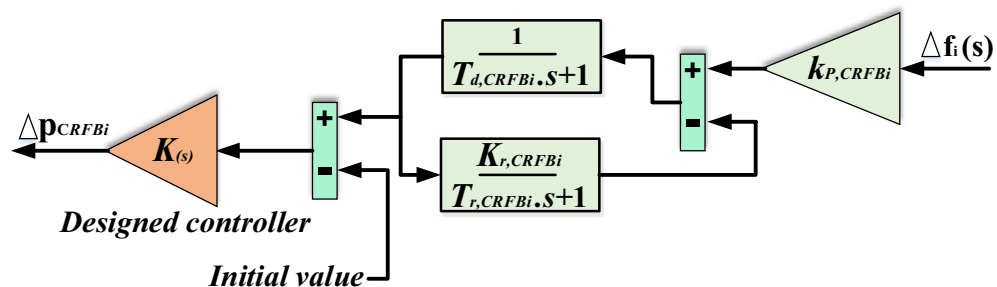


Figure 7. CRFBs unit's transfer function model⁴⁵.

exactly the same, with one significant difference. Instead of the proportional component, the TID controller incorporates a tilted component with a transfer function of $s^{-(1/n)}$, where n represents the FOCs. The TID controller has numerous benefits over a typical PID controller. It exhibits better disturbance rejection, simplified tuning process, and reduced sensitivity to variations in system parameters, resulting in improved dynamic response. Additionally, another type of FOCs called the fractional-order-integral-derivative (FO-ID) controller is available, which offers enhanced system performance and flexibility. Thus, this study replaced the second and third gains in TID controller by the FO-I and FO-D terms to attain the $T I^\lambda D^\mu$ controller. Where the frequency fluctuations of the area (Δf_i) attends as the $T I^\lambda D^\mu$ controller's input signal. Furthermore, the mathematical expression of $T I^\lambda D^\mu$ controller is expressed according to the next equation:

$$T I^\lambda D^\mu (s) = \frac{K_{ti,i}}{s^{1/n}} + \frac{K_{i,i}}{s^\lambda} + K_{d,i} s^\mu \tag{9}$$

The constraints of gain values, $k_{ti,i(TI^\lambda D^\mu)}$, $k_{i,i(TI^\lambda D^\mu)}$, $k_{d,i(TI^\lambda D^\mu)}$, $n_{(TI^\lambda D^\mu)}$, $\lambda_{(TI^\lambda D^\mu)}$, and $\mu_{(TI^\lambda D^\mu)}$ utilized in this work in both areas of the considered power grid are expressed as follows:

$$k_{ti,i(TI^\lambda D^\mu)^{max}} \geq k_{ti,i(TI^\lambda D^\mu)} \geq k_{ti,i(TI^\lambda D^\mu)^{min}} \tag{10}$$

$$k_{i,i(TI^\lambda D^\mu)^{max}} \geq k_{i,i(TI^\lambda D^\mu)} \geq k_{i,i(TI^\lambda D^\mu)^{min}} \tag{11}$$

$$k_{d,i(TI^\lambda D^\mu)^{max}} \geq k_{d,i(TI^\lambda D^\mu)} \geq k_{d,i(TI^\lambda D^\mu)^{min}} \tag{12}$$

$$n_{(TI^\lambda D^\mu)^{max}} \geq n_{(TI^\lambda D^\mu)} \geq n_{(TI^\lambda D^\mu)^{min}} \tag{13}$$

$$\lambda_{(TI^\lambda D^\mu)^{max}} \geq \lambda_{(TI^\lambda D^\mu)} \geq \lambda_{(TI^\lambda D^\mu)^{min}} \tag{14}$$

$$\mu_{(TI^\lambda D^\mu)^{max}} \geq \mu_{(TI^\lambda D^\mu)} \geq \mu_{(TI^\lambda D^\mu)^{min}} \tag{15}$$

where i refers scheme of the suggested controller for each of the three mentioned traditional power plants; thus, ($i=1, 2, 3$). The gain values ($k_{ti,i(TI^\lambda D^\mu)}$, $k_{i,i(TI^\lambda D^\mu)}$, $k_{d,i(TI^\lambda D^\mu)}$, $n_{(TI^\lambda D^\mu)}$, $\lambda_{(TI^\lambda D^\mu)}$, and $\mu_{(TI^\lambda D^\mu)}$) are chosen between $[0, 10]$, $n_{(TI^\lambda D^\mu)}$ is set among the range $[1, 10]$, the fractional derivative ($\mu_{(TI^\lambda D^\mu)}$) and fractional integrator ($\lambda_{(TI^\lambda D^\mu)}$) orders are chosen among the range $[0, 1]$.

Additionally, Fig. 8 illustrates the proposed controller structure for the three considered generating units. Where, the considered controller has dual inputs: the ACE value and the derivative value of ACE. The scalability variables for the inputs are symbolized as K_1 and K_2 , while the scalability variables for the output are symbolized as K_3 and K_4 . Traditionally, determining these scaling factors has been a challenge, often relying on trial-and-error methods. This can make obtaining optimal parameter values that improve system performance difficult. However, this study overcomes this limitation by designing the considered (fuzzy-PID) + ($T I^\lambda D^\mu$) controller. Furthermore, the COA algorithm is used to determine these optimized values, where, the fuzzy membership function can be either triangular or Gaussian shape. In practical applications of electrical systems, triangular membership is often preferred due to its computational efficiency and simplicity. It is a first-order function of

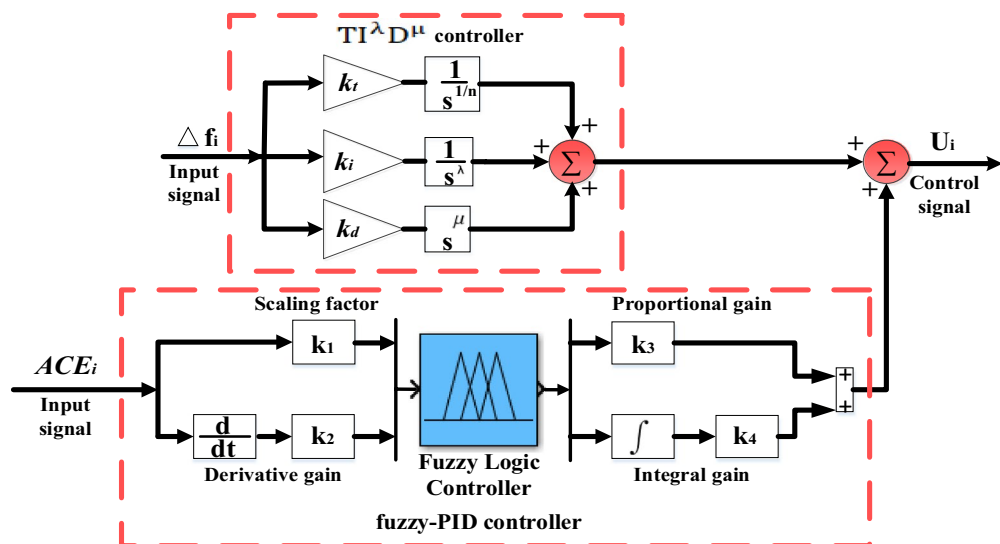


Figure 8. Considered (fuzzy-PID) + ($T I^\lambda D^\mu$) controller arrangement.

mathematics that decreases computational load. Triangular membership functions are typically used with PID controllers and exhibit abundantly symmetric characteristics in both output as well as input. Furthermore, the mathematical expression of (fuzzy-PID) controller is expressed according to the following equation:

$$\text{fuzzy - PID}(s) = K_{1,i} + K_{3,i} + \frac{K_{4,i}}{s} + K_{2,i}s \tag{16}$$

The constraints of gain values, $K_{1,i}$, $K_{2,i}$, $K_{3,i}$, and $K_{4,i}$ utilized in this work in both areas of the analyzed power grid are expressed as follows:

$$k_{1,i(\text{fuzzy-PID})}^{\max} \geq k_{1,i(\text{fuzzy-PID})} \geq k_{1,i(\text{fuzzy-PID})}^{\min} \tag{17}$$

$$k_{3,i(\text{fuzzy-PID})}^{\max} \geq k_{3,i(\text{fuzzy-PID})} \geq k_{3,i(\text{fuzzy-PID})}^{\min} \tag{18}$$

$$k_{4,i(\text{fuzzy-PID})}^{\max} \geq k_{4,i(\text{fuzzy-PID})} \geq k_{4,i(\text{fuzzy-PID})}^{\min} \tag{19}$$

$$k_{2,i(\text{fuzzy-PID})}^{\max} \geq k_{2,i(\text{fuzzy-PID})} \geq k_{2,i(\text{fuzzy-PID})}^{\min} \tag{20}$$

The gain values ($k_{1,i(\text{fuzzy-PID})}$, $k_{2,i(\text{fuzzy-PID})}$, $k_{3,i(\text{fuzzy-PID})}$, and $k_{4,i(\text{fuzzy-PID})}$) are chosen between [0, 10].

The decision about the choice of fuzzy control settings is influenced by the specific characteristics of the system under consideration as well as the designer’s expertise. The range of fuzzy function memberships is determined by predicting the system’s input and output discourse universes. Typically, a decision-maker defines the acceptable risk level for the output and input variables. In this study, the range intervals are selected between -1 and 1, as deviations beyond this range are not necessary to achieve system stability. Symmetric triangular membership functions with 50% overlap are recommended, and a tuning procedure can be applied to adjust the spread and overlap as needed to achieve satisfactory results. In this study, the fuzzy-PID controller in this work utilizes five triangular membership functions: negative big (NB), negative small (NS), zero (Z), positive small (PS), and positive big (PB). These membership functions, depicted in Fig. 9, are utilized for outputs as well as inputs. Consequently, the fuzzy-PID controller requires 25 rules to generate fuzzy outputs, which play a crucial role in its performance. These rules are presented in Table 3. Also, the arrangement of the considered combination of (fuzzy-PID) and ($T I^\lambda D^\mu$) controller is depicted in Fig. 8. According to various published studies, the load frequency controller’s input signal is usually ACE. In this study, the authors proposed (fuzzy-PID) + (T

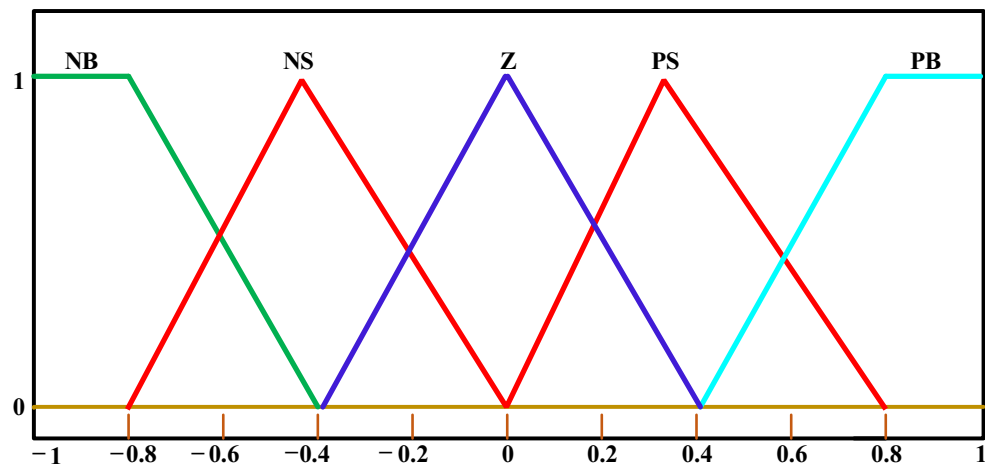


Figure 9. The triangular membership functions of the FLC’s input and output.

ACE	dACE/dt				
	NB	NS	Z	PS	PB
NB	NB	NB	NB	NS	Z
NS	NB	NB	NS	Z	PS
Z	NB	NS	Z	PS	PB
PS	NS	Z	PS	PB	PB
PB	Z	PS	PB	PB	PB

Table 3. Rule base of the FLC.

I^2D^μ) controller, which combines two concepts. The first (fuzzy-PID) controller term receives the *ACE* signal as an input. The extra ($T I^2D^\mu$) controller term employs the Δf signal to improve system performance. It is obviously true that the total arrangement of the proposed controller demonstrates superior rejection of existing disturbances by mitigating all low- and high-frequency disturbances^{4,6}.

In this study, the authors propose the utilization of the integral time absolute error (*ITAE*) criteria as a means for minimizing the value of the cost function. Optimizing development is improved by adding the element of a time term to the *ITAE* criteria and the system constancy will be more enhanced compared to using the integral of squared error (*ISE*) criteria. Increased efficacy in error reduction is achieved by multiplying the factor of time by the integral of the absolute error. The *ITAE* principles can be expressed as follows:

$$J = ITAE = \int_0^{Tsim} t \cdot [|\Delta f_a| + |\Delta f_b| + |\Delta p_{tie}|] \cdot dt \tag{21}$$

Where *J* denotes the value of proposed cost function which seeks to be the lowest possible value in this work, $|\Delta f_a|$ represents the area-a frequency waveform’s absolute error, $|\Delta f_b|$ represents the area-b frequency waveform’s absolute error, $|\Delta p_{tie}|$ represents the tie-line’s power flow change absolute error, *Tsim* denotes the overall simulation runtime, and the variable *dt* symbolizes the error signal sampling period throughout the simulation procedure.

The crayfish optimization algorithm (COA)

The Crayfish Optimization Algorithm (COA) principles which is proposed by Heming et.al is discussed in detail in this section⁴⁰. Foraging, competition, and summer resort behaviors are the three crayfish behaviors that the COA simulates. To equilibrium the algorithm’s exploration and exploitation features, these behaviors are classified into three stages of actions (i.e., summer resort, competition, and foraging). The summer resort stage symbolizes the COA’s exploring phase, while the competition and foraging stages indicate the exploitation phase. The temperature has an effect on the algorithm’s exploration and exploitation. The initial stage of the algorithm defines a crawfish colony, denoted as *X*, where *X_i* indicates a solution and describes the position of the *i*th crayfish. ($X_i = \{X_{i,1}, X_{i,2}, X_{i,3} \dots X_{i,dim}\}$, *dim* is the dimension which denotes the optimization problem’s characteristic quantity. Random constants that represent the ambient temperature have an influence on individual’s behavior. When the temperatures increase, the COA moves into the stage of summer resort or the competition stage. New solutions are updated at the summer resort stage depending on the position of an individual, *X_i* and the position of cave, *X_{shade}*. When the ambient temperature is appropriate and warm enough, the COA begins the foraging stage. During this stage, the best location, likewise regarded as an optimal solution, reveals the location of food. The *fitness_i* value of the current solution (gained through *X_i*) and the optimal solution *fitness_{food}* value (gained as a result of the optimal solution) define the size of the food. During foraging, crayfish obtain new solutions by considering their position, *X_i* a food intake constant *p*, and the update of the food position *X_{food}*. If crayfish want to eat food that is excessively large for them, they will first break it down with their claw foot before alternating between their second and third walking feet. Overall, the COA simulates crayfish behavior by incorporating exploration and exploitation through temperature regulation, updating solutions based on individual and optimal positions, and considering the size and consumption of food.

This subsection summarizes the methodology of the COA algorithm:

Initialization process of COA

This study proposes a controller with both lower and upper limits for parameters. To accomplish the global goal, the population of the COA method is formed between these boundaries using main mathematical procedures. The population of the COA method can be expressed using Eq. (22).

$$X_{i,j} = rand \times (UB_j - LB_j) + LB_j \tag{22}$$

Where *X_{i,j}* represents where the individual *i* is located in the *j* dimension, *LB_j* represents the *j*th dimension’s lower bound, *UB_j* represents the *j*th dimension’s upper bound, and *rand* is a random number.

The COA method starts by generating candidate solutions (*X*) randomly. In each iteration, the obtained solution that is closest to the global goal (target) represents the optimal solution. The obtained solutions’ positions are indicated in the next matrix.

$$X = \begin{bmatrix} X_{1,1} & X_{1,j} & \dots & X_{1,dim} \\ X_{i,1} & X_{i,j} & \dots & X_{i,dim} \\ \vdots & \vdots & \ddots & \vdots \\ X_{N,1} & X_{N,j} & \dots & X_{N,dim} \end{bmatrix} \tag{23}$$

where *X* refers the initial population position, *N* refers the population number, *dim* refers the population dimension.

The fitness solution, which represents the solution with the best fitness value among the obtained solutions, is calculated as following:

$$f_{fitness} = [f_1 f_2 f_3 \dots \dots \dots f_N]^T \tag{24}$$

Definition of the crayfish temperature and its intake

The behavior of crayfish is influenced by changes in temperature, which determine the stage they enter. Temperature is determined by Eq. (25). When the temperature exceeds 30 °C, crayfish will seek out cooler areas for taking a summer vacation. Crayfish will begin to forage when the temperature is appropriate. Temperature influences the amount of food consumed by crayfish. Crayfish prefer temperatures between 15 °C and 30 °C for feeding, with 25 °C being the most favorable. Equation (26) provides the mathematical representation of the crayfish intake.

$$Temp = rand \times 15 + 20 \quad (25)$$

In this equation, "Temp" denotes the temperature of the crayfish's environment.

$$p = C_1 \times \left(\frac{1}{\sqrt{2 \times \pi} \times \sigma} \times \exp\left(-\frac{(Temp - \mu)^2}{2\sigma^2}\right) \right) \quad (26)$$

Among them, σ and C_1 is used to regulate crayfish intake at various temperatures, while μ refers to the optimal crayfish temperature.

The exploration stage (summer resort stage)

When the temperature exceeds 30 °C, it is considered too high, and crayfish will choose to seek refuge in caves to take the period of summer vacation. The cave X_{shade} is identified as listed below:

$$X_{shade} = (X_G + X_L)/2 \quad (27)$$

In this scenario, X_G demonstrates the optimal position attained so far throughout iterations, while X_L represents the current population's optimal position.

The competition among crayfish for caves is a random occurrence. When a randomly generated number $rand < 0.5$, it means that there aren't any other crayfish fighting for caves. In such instances, the crayfish are going to move directly to the cave for their break during the summer vacation. This behavior is governed by Eq. (28).

$$X_{ij}^{t+1} = X_{ij}^t + C_2 \times rand \times (X_{shade} - X_{ij}^t) \quad (28)$$

Where t refers the current iteration number, and $t+1$ refers the number of the next generation iteration, C_2 refers the decreasing curve, as proved by Eq. (29).

$$C_2 = 2 - (t/T) \quad (29)$$

where t indicates the maximum iterations' number.

Crayfish's goal at the summer resort stage is to go close to the cave, which represents the optimal solution. Consequently, crayfish will move towards the cave in an effort to get closer to the optimal solution. Individuals become closer to the best solution through this process, which also improves the COA algorithm's exploitation capability, thus allowing for faster convergence.

The exploitation stage (competition stage)

When the temperature exceeds 30 °C and $rand \geq 0.5$, it indicates that other crayfish are also captivated by the cave. In this situation, they will engage in a competitive fight to gain access to the cave. As per Eq. (30), the crayfish competes over the cave:

$$X_{ij}^{t+1} = X_{ij}^t - X_{zj}^t + X_{shade} \quad (30)$$

Where z sums up the crayfish's arbitrarily individual, as demonstrated in Eq. (31):

$$z = \text{round}(rand \times (N - 1) + 1) \quad (31)$$

Crayfish compete over the cave during the competition stage. Each crayfish, denoted as X_i , adjusts its position depending on where another crayfish is located, X_z as described in Eq. (30). This adjustment of positions expands the search range of the COA algorithm, enhancing its exploration ability.

The exploitation stage (foraging stage)

When the $Temp \leq 30$ °C, it seems to be appropriate for feeding crayfish. In this case, the crayfish will keep moving in the direction of the food supply. Once they find the food, crayfish will assess its size. Crayfish will use their claws to rip apart food if it is deemed to be excessively large. Then, they will alternately use their two remaining walking feet to consume their food. Food location, denoted as X_{food} , is defined as follows:

$$X_{food} = X_G \quad (32)$$

The food size Q is defined as:

$$Q = C_3 \times rand \times (\text{fitness}_i / \text{fitness}_{food}) \quad (33)$$

Here, C_3 refers the factor of food, which represents the largest food size and has a constant value of 3. " fitness_i " refers the i th crayfish's fitness value, while " fitness_{food} " refers the food location's fitness value. The crayfish uses the

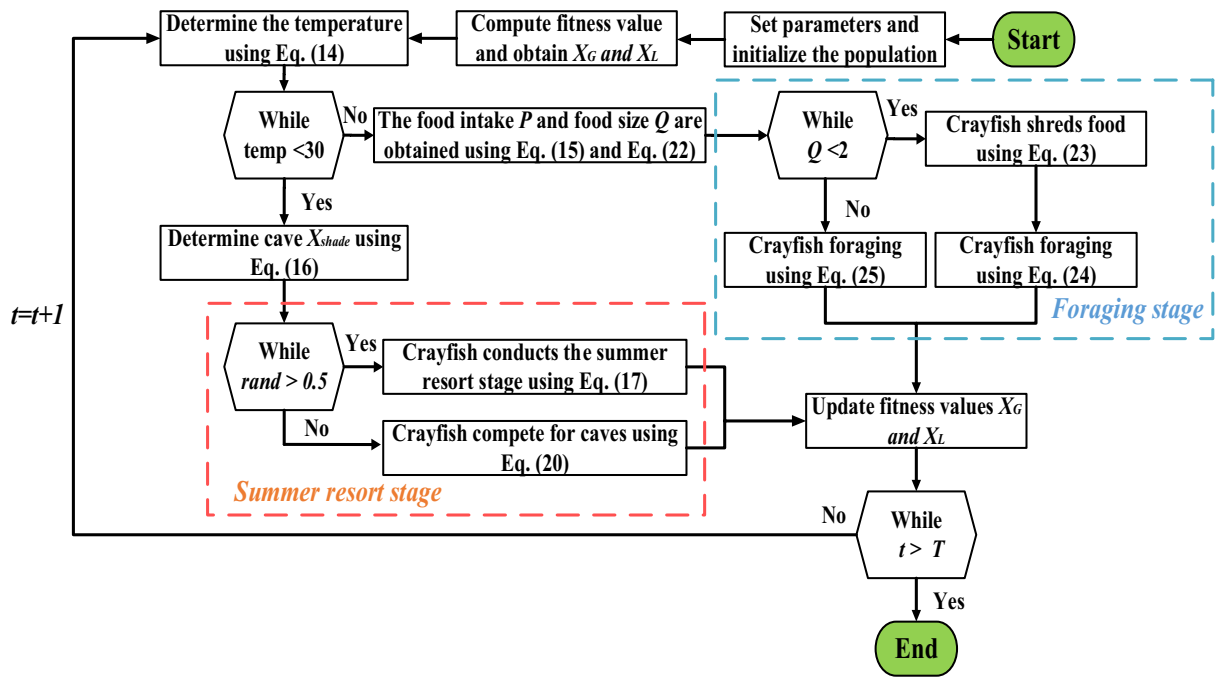


Figure 10. The flow chart of the COA algorithm⁴⁰.

largest food’s quantity as a benchmark for determining the size of food. When Q surpasses $(C_3+1)/2$, it implies a large amount of the food. Here, the crayfish is going to utilize their first claw foot for ripping the food. The mathematical equation representing this action is provided as follows:

$$X_{food} = \exp\left(\frac{-1}{Q}\right) \times X_{food} \tag{34}$$

This mechanism enables crayfish to adapt their feeding behavior depending on the size of the food available, ensuring efficient consumption and utilization of resources.

When the food becomes crumbly and smaller, the crayfish will pick it up with their second and third paws alternatively and put it in their mouth. A sine and cosine function combination is utilized to describe this alternating process. Furthermore, the crayfish’s food intake is related to the food they get. Foraging is calculated as follows:

$$X_{i,j}^{t+1} = X_{i,j}^t + X_{food} \times p \times (\cos(2 \times \pi \times rand) - \sin(2 \times \pi \times rand)) \tag{35}$$

When $Q \leq (C_3+1)/2$, the crayfish only needs to proceed forward to the food and devour it immediately. The equation for this behavior is provided as follows:

$$X_{i,j}^{t+1} = (X_{i,j}^t - X_{food}) \times p + p \times rand \times X_{i,j}^t \tag{36}$$

Crayfish use a variety of feeding strategies during the foraging stage, which are determined by their food size, denoted as Q . The food location X_{food} represents the optimal solution in this context. If the food Q ’s size is appropriate for crayfish feeding, they will approach the food and consume it. However, if Q is too large, it shows that there is a significant difference between the optimal solution and the crayfish. In such cases, X_{food} needs to be adjusted to reduce the difference as well as moving it up close to the food. Furthermore, the randomness of the crayfish food intake enhancement algorithm is under executive control. This ensures that the crayfish can approach the optimal solution more effectively during the foraging stage. Through this process, the COA algorithm gradually converges towards the optimal solution, enhancing its exploitation ability and achieving good convergence performance. Here, Fig. 10 depicts the COA method’s flowchart.

Ethical approval

This article does not contain any studies with human participants or animals performed by any of the authors.

Execution and results discussion

In this work, a supplementary control scheme called (fuzzy-PID) + $(T I^\lambda D^\mu)$ is proposed as well as implemented for the analyzed power grid. According to the merits of fuzzy logic and fractional order schemes, the proposed controller outperforms superior rejection of existing disturbances by dampening all low- and high-frequency disruptions. This present study addresses the presence of high renewables penetration in the power grid. Multiple scenarios are scrutinized to evaluate how well the suggested control approach coordinates several different

controllers. The proposed algorithm's performance is additionally assessed in comparison to different techniques. To optimize the suggested controller, the COA technique is employed to alleviate system frequency excursions. The simulations are conducted using MATLAB/SIMULINK® program (R2016a) on a computer with specific hardware specifications. For optimizing the proposed control structure, an m-file containing the original COA algorithm code and paired with the stipulated power grid model is employed. The several simulation scenarios are executed on a PC with the following specifications: 8.00 GB of RAM with a 2.60 GHz Intel Core i5 processor. Furthermore, the frequency stability assessing takes into consideration varied operational conditions in the scenarios listed below:

- Scenario A* Evaluating the analyzed power grid's performance with different varied load pattern profiles.
- Scenario B* Evaluating the examined power grid's performance involving high renewables penetration, aiming to examine the grid's capability to handle this issue.
- Scenario C* Evaluating the suggested controller's robustness in real-time for stability and reliability using the IEEE-39 bus system. The validation includes considering the impact of SLD.
- Scenario D* Evaluating the efficacy of the recommended controller utilizing a real-time IEEE-39 bus system, considering high renewables penetration within the system, to assess its effectiveness with the goal to attain dependability and stability.
- Scenario E* Evaluating the performance of the proposed controller under varying CDT conditions before and after the LFC in the IEEE-39 bus system. This evaluation also considers high renewable energy penetrations.
- Scenario F* Evaluating the proposed strategy's effectiveness by comparing the effectiveness of the IEEE 39 buses system with and without the proposed strategy, considering high renewables penetration.
- Scenario G* Stability analysis of the proposed (fuzzy-PID) + ($T I^\lambda D^\mu$) controller.

When optimizing the proposed (fuzzy-PID) + ($T I^\lambda D^\mu$) controller using the COA algorithm, certain arrangements should be considered. These include employing 30 search agents and performing 50 iterations. Figure 11 shows the obtained convergence curve, which provides insights into the investigated power grid's performance with the recommended COA-based controller. It should be noted that the presented convergence curve in the figure is obtained assuming a 1% SLD occurring to area-a at $t = 10$ s within the examined power grid, without considering a high renewables penetration. Whereas, the behavior of proposed controller based on COA is summarized as beginning with a value of the objective function near 0.00201 and dropping with each attempt until it achieves a value near 0.00188.

Scenario A Evaluating the analyzed power grid's performance with different varied load pattern profiles.

The following scenario is intended to provide an initial comparison for accurately verifying the suggested controller's efficiency and algorithm in achieving frequency stabilization of the analyzed power grid. To conduct a more detailed analysis, a comparison is made among various aforementioned published controllers.

Case A.1 In this case, it is assumed that area-a of the assessed power grid includes a step load. The purpose is to assess the effectiveness of the COA algorithm in addressing the frequency stability issue through the use of the supplementary control loop. Assuming a step load of 1% magnitude at $t = 10$ s, representing either the disconnection of generation power plants or the disconnection of a variety of electrical loads. The obtained controller parameters for the proposed controller and the other mentioned controllers are presented in Table 4. Additionally, the system's performance is depicted in Fig. 12.

The values of maximum overshoots (O_{sh}) and maximum undershoots (U_{sh}) obtained from the various considered dynamic responses of the analyzed power grid using the recommended controller relied on the COA method are considerably lower than the results obtained with other mentioned controllers via various different

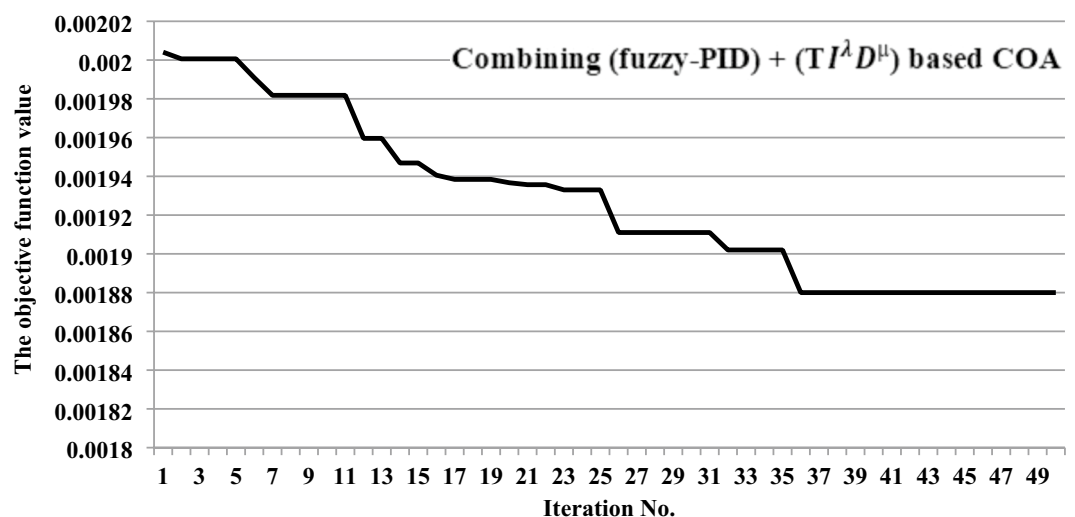


Figure 11. Obtained convergence curve of the suggested controller tuned by the COA method.

Controller structures	Thermal unit	Hydro unit	Gas unit	Objective function value (ITAE)
PID-optimized via AOA ¹⁸	$k_p=10, k_i=1.5975, k_d=2.7449$	$k_p=1.5975, k_i=0.0837, k_d=0.0875$	$k_p=10, k_i=10, k_d=1.2779$	0.189
FOPID-optimized via ESAOA ¹⁸	$k_p=8.9645, k_i=9.9979, k_d=9.7397, \lambda=0.7266, \mu=0.8519$	$k_p=6.6278, k_i=9.1570, k_d=4.631, \lambda=0.587, \mu=0.0887$	$k_p=9.7594, k_i=9.9997, k_d=7.976, \lambda=0.9159, \mu=0.3775$	0.1233
PD-PI- optimized via HHO ³	$k_{p1}=5, k_{d1}=5, k_{p2}=5, k_{i1}=5$	$k_{p1}=5, k_{d1}=0.4447, k_{p2}=5, k_{i1}=-2.6257$	$k_{p1}=5, k_{d1}=-5, k_{p2}=5, k_{i1}=5$	0.04312
FO-(PD-PI)- optimized via MRFO ³	$k_{p1}=8.4889, k_{d1}=4.7798, \mu=0.888, k_{p2}=3.3705, k_{i1}=9.1858, \lambda=0.63405$	$k_{p1}=8.3087, k_{d1}=7.8085, \mu=0.4372, k_{p2}=7.6906, k_{i1}=9.3538, \lambda=0.13835$	$k_{p1}=0.4128, k_{d1}=4.8394, \mu=0.6828, k_{p2}=1.8088, k_{i1}=0.95754, \lambda=0.82713$	0.03477
Fuzzy-PID+ (T ¹ D ⁿ)- optimized via COA	$k_1=10, k_2=9.9229, k_3=6.923, k_4=10, k_i=10, k_i=9.9827, k_d=5.3442, \lambda=0.7279, \mu=1 \times 10^{-8}, n=4.682$	$k_1=9.9962, k_2=10, k_3=9.984, k_4=4.039, k_i=5.5703, k_i=10, k_d=9.987, \lambda=0.3176, \mu=0.3844, n=1$	$k_1=10, k_2=9.9846, k_3=7.561, k_4=1.6455, k_i=6.771, k_i=9.9041, k_d=8.2064, \lambda=0.8804, \mu=1 \times 10^{-8}, n=4.25$	0.00188

Table 4. Optimal values of various optimized controllers.

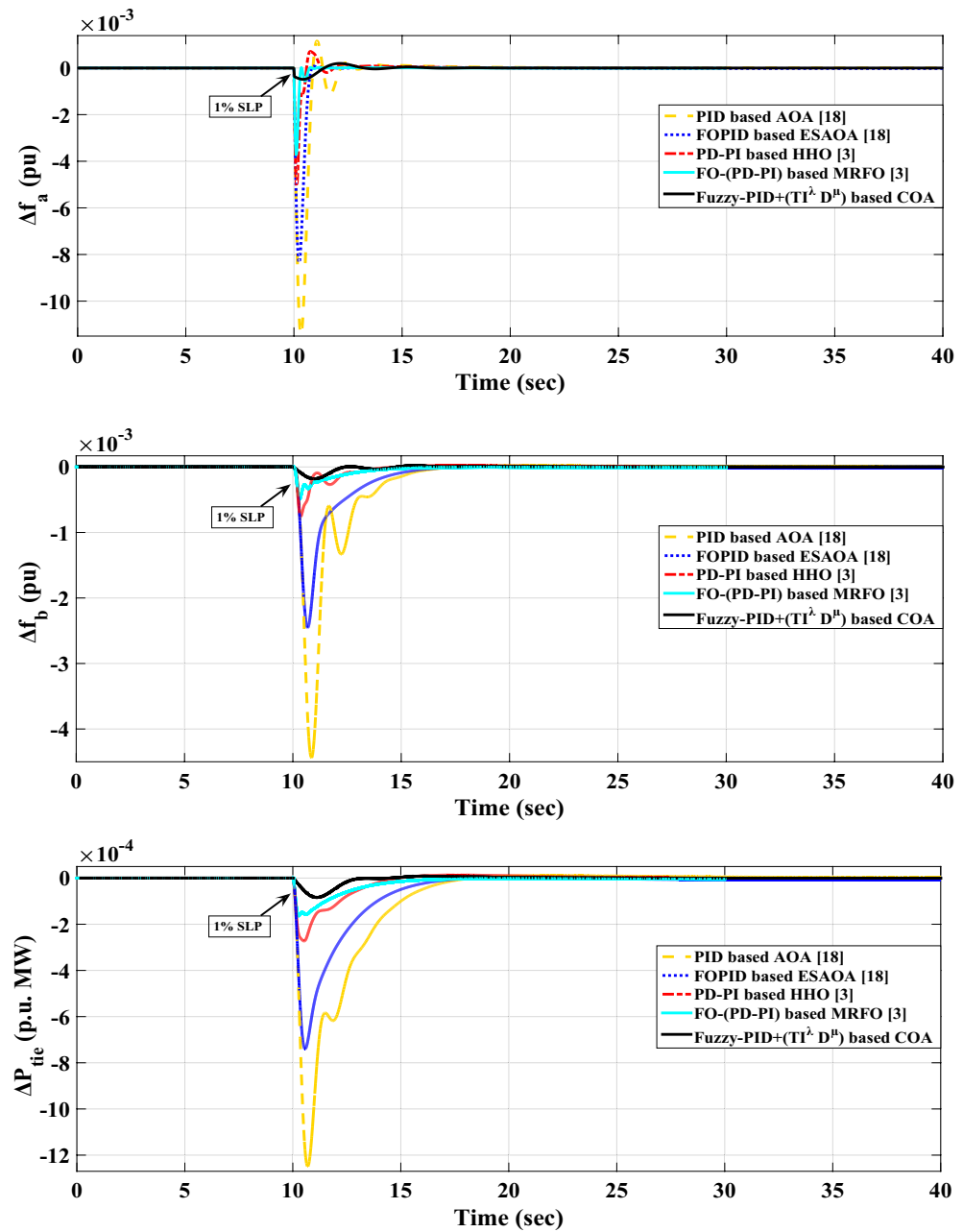


Figure 12. LFC controllers' dynamic responses to step load disruption for Case A.1.

Controller structures	Considered dynamic response of (Δf_a)	Considered dynamic response of (Δf_b)	Considered dynamic response of (ΔP_{tie})
PID-optimized via AOA ¹⁸	$O_{sh} = 1.158$	$O_{sh} = 0.0209$	$O_{sh} = 0.01107$
	$U_{sh} = -11.42$	$U_{sh} = -4.443$	$U_{sh} = -1.249$
FOPID-optimized via ESAOA ¹⁸	$O_{sh} = 0.0802$	$O_{sh} = 0.0018$	$O_{sh} = 0.00109$
	$U_{sh} = -8.344$	$U_{sh} = -2.456$	$U_{sh} = -0.7403$
PD-PI-optimized via HHO ³	$O_{sh} = 0.7113$	$O_{sh} = 0.02308$	$O_{sh} = 0.0137$
	$U_{sh} = -5.06$	$U_{sh} = -0.760$	$U_{sh} = -0.2735$
FO-(PD-PI)-optimized via MRFO ³	$O_{sh} = 0.0249$	$O_{sh} = 0$	$O_{sh} = 0$
	$U_{sh} = -3.734$	$U_{sh} = -0.4837$	$U_{sh} = -0.1623$
Fuzzy-PID + ($T I^2 D^\mu$)-optimized via COA	$O_{sh} = 0.1983$	$O_{sh} = 0.0203$	$O_{sh} = 0.0083$
	$U_{sh} = -0.4975$	$U_{sh} = -0.1839$	$U_{sh} = -0.08528$

Table 5. Specifications of the analyzed system’s transient response for scenario A.1. All values are multiplied by (10^{-3}).

Controller structures	Δf_a		Δf_b		ΔP_{tie}	
	U_{sh}	O_{sh}	U_{sh}	O_{sh}	U_{sh}	O_{sh}
FOPID-optimized via ESAOA ¹⁸	26.93	93.07	44.72	91.39	40.73	90.15
PD-PI-optimized via HHO ³	55.69	38.58	82.89	10.43	78.1	23.76
FO-(PD-PI)-optimized via MRFO ³	67.3	97.84	89.11	100	87	100
Fuzzy-PID + ($T I^2 D^\mu$)-optimized via COA	95.64	82.88	95.86	2.87	93.17	25.02

Table 6. Percentage improvements in O_{sh} and U_{sh} for Case A.1. Optimal percentage values are highlighted in bold format.

techniques, as shown in Fig. 12. Furthermore, Table 5 provides an in-depth overview of the system performance in Case A.1. Then, Table 6 further highlights the percentage improvements in O_{sh} and U_{sh} for this specific case, illustrating the enhancements achieved compared to the previous controllers.

Case A.2 A series SLD pattern is applied in this case to assess the performance of the proposed (fuzzy-PID) + ($T I^2 D^\mu$) controller. This pattern involves a succession of forced switches of generators or outages of connected loads, which can potentially lead to power grid instability. Figure 13 depicts the series SLD form. Then, Fig. 14 presents the system’s various dynamic responses for this case.

Figure 14 illustrates that the maximum O_{sh} and maximum U_{sh} values obtained from the system’s dynamic responses using the proposed (fuzzy-PID) + ($T I^2 D^\mu$) controller relied on COA are significantly lower than the results obtained from the aforementioned published controllers. Furthermore, Table 7 provides the precise values of O_{sh} and U_{sh} for the power flowing in the tie-line and frequencies for both areas. Additionally, Table 8 highlights the system’s overall improvement percent achieved in this case.

Case A.3 Additionally, in area-a of the analyzed power grid, a random load fluctuation form is assumed, occurring at $t = 100$ s. This form represents a wide range of disruptions in series in industrially interconnected loads, producing similar grid effects, such as grid instability and the occurrence of blackouts. Figure 15 clarifies the applicable RLD pattern. Furthermore, Fig. 16 provides a comparative analysis of the examined power grid’s

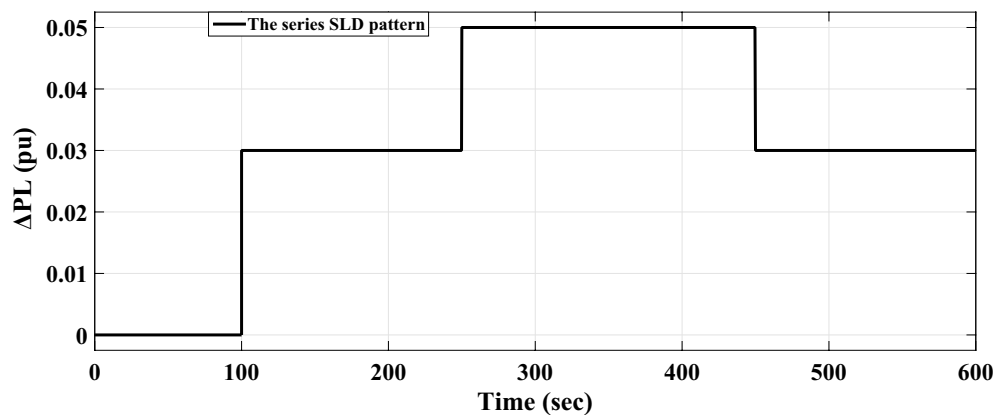


Figure 13. The implemented area-a series SLD form.

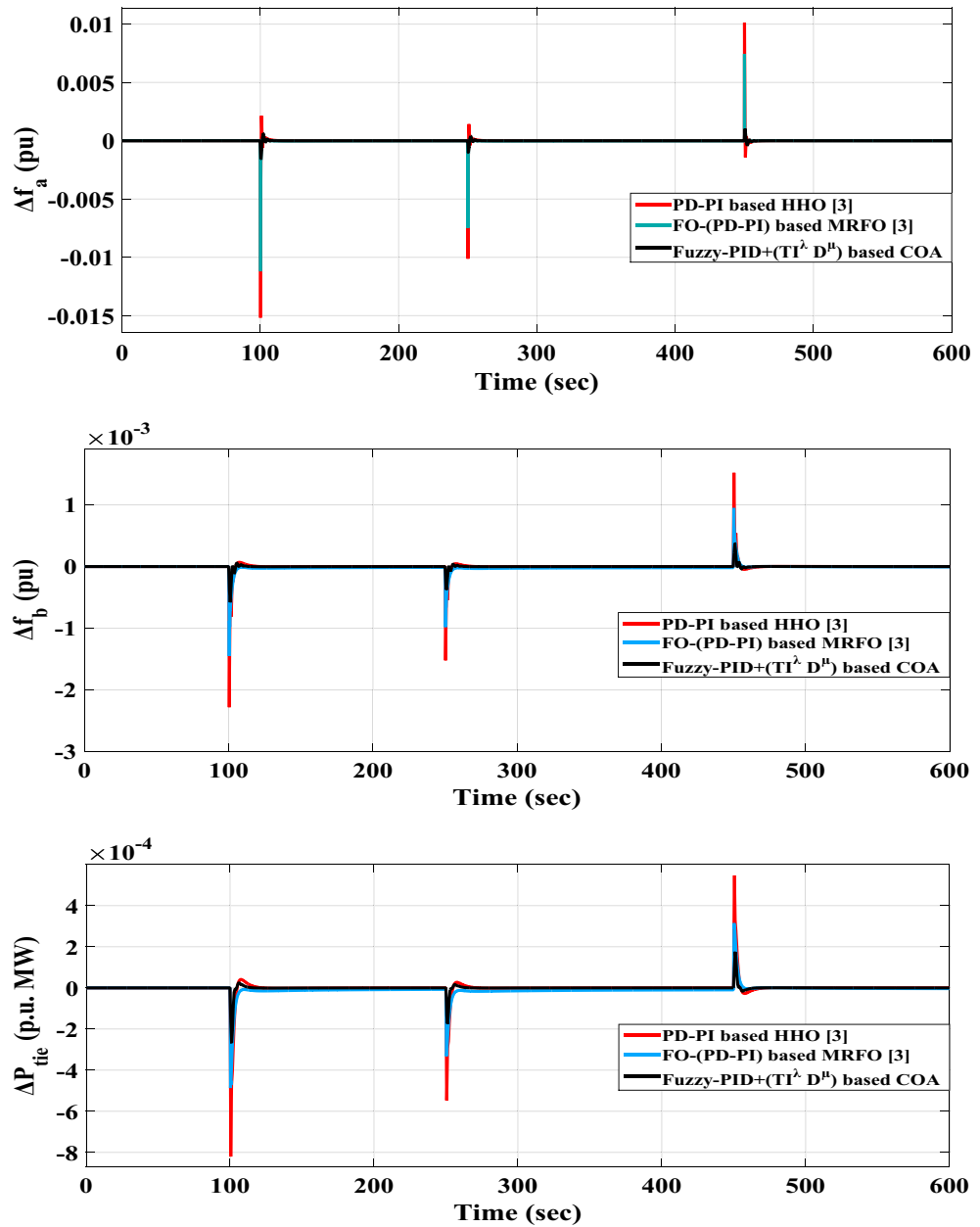


Figure 14. LFC controllers' dynamic responses to series step load disruption for Case A.2.

Controller structures	Considered dynamic response of (Δf_a)	Considered dynamic response of (Δf_b)	Considered dynamic response of (ΔP_{tie})
PD-PI-optimized via HHO ³	$O_{sh} = 10.121$	$O_{sh} = 1.52$	$O_{sh} = 0.5469$
	$U_{sh} = -15.181$	$U_{sh} = -2.28$	$U_{sh} = -0.82035$
FO-(PD-PI)-optimized via MRFO ³	$O_{sh} = 7.45$	$O_{sh} = 0.94914$	$O_{sh} = 0.31477$
	$U_{sh} = -11.203$	$U_{sh} = -1.451$	$U_{sh} = -0.48686$
Fuzzy-PID + ($T I^\lambda D^\mu$)-optimized via COA	$O_{sh} = 1.12$	$O_{sh} = 0.3051$	$O_{sh} = 0.1670$
	$U_{sh} = -1.817$	$U_{sh} = -0.5570$	$U_{sh} = -0.2364$

Table 7. Specifications of the analyzed system's transient response for scenario A.2. All values are multiplied by (10^{-3}).

Controller structures	Δf_a		Δf_b		ΔP_{tie}	
	U_{sh}	O_{sh}	U_{sh}	O_{sh}	U_{sh}	O_{sh}
FO-(PD-PI)-optimized via MRFO ³	26.2	26.39	36.36	37.56	40.65	42.44
Fuzzy-PID+(T I ^λ D ^μ)-optimized via COA	88.03	88.93	75.57	79.93	71.18	69.46

Table 8. Percentage improvements in O_{sh} and U_{sh} for Case A.2. Optimal percentage values are highlighted in bold format.

dynamic performance according to the recommended controller scheme and the other two aforementioned controllers.

Figure 16 shows that the maximum O_{sh} and maximum U_{sh} values obtained from the considered power grid’s dynamic responses utilizing the recommended (fuzzy-PID) + (T I^λD^μ) controller relied on COA are significantly lower than the values obtained from the aforementioned published controllers. Furthermore, Table 9 shows the precise values of O_{sh} and U_{sh} for the power flowing in the tie-line and frequencies for both areas. Table 10 also shows the system’s overall improvement percent.

Scenario B Evaluating the examined power grid’s performance involving high renewables penetration, aiming to examine the grid’s capability to handle this issue.

The scenario’s purpose is to examine the disturbances caused by a significant penetration of renewables in both of the analyzed power grid’s areas. Specifically, area-a has been incorporated by 10 windmills and 10 PV power plants at 100 min and 400 min, respectively, utilizing a random demand fluctuation pattern. In area-b, the identical integration parameters for the penetration of renewables are applied; PV power plants integrate at 700 min and windmills at 600 min. The generated power from the RESs integrated into the analyzed power grid, as well as various system dynamic responses, are elucidated in Figs. 17,18, respectively.

Furthermore, Table 11 shows the different acquired values of O_{sh} and U_{sh} for the power flowing in the tie-line and frequencies for both areas applying all of the previously mentioned controllers. Table 12 also clarifies the system’s overall improvement percent for this case.

Scenario C: Evaluating the suggested controller’s robustness in real-time for stability and reliability using the IEEE-39 bus system. The validation includes considering the impact of SLD.

For evaluating the suggested (fuzzy-PID) + (T I^λD^μ) controller approach for load frequency management, the standard real-world New England IEEE-39 bus system is applied in this scenario. The standard real-world New England IEEE-39 bus system consists of ten reheat thermal generators, nineteen loads, thirty-eight transmission lines, and twelve transformers, as shown in Fig. 19. The system is divided into three interconnected areas, namely area 1, area 2, and area 3, with respective rated area power capacities of $P_{r1} = 1500MW$, $P_{r2} = 2000MW$, and $P_{r3} = 1500MW$. Appendix B provides the system parameter values. In this approach, each area’s generating units are substituted with a single equivalent generation unit. The following equations are used to calculate the equivalent inertia constant and speed regulation parameters⁵⁴:

$$H_{eqv} = \frac{H_1S_1 + H_2S_2 + \dots + H_nS_n}{S_{system}} \tag{37}$$

$$R_{evq} = \frac{1}{\frac{1}{R_1} \left(\frac{S_1}{S_{system}} \right) + \frac{1}{R_2} \left(\frac{S_2}{S_{system}} \right) + \dots + \frac{1}{R_n} \left(\frac{S_n}{S_{system}} \right)} \text{HZ/MW}_{pu} \tag{38}$$

$$S_{system} = S_1 + S_2 + \dots + S_n \tag{39}$$

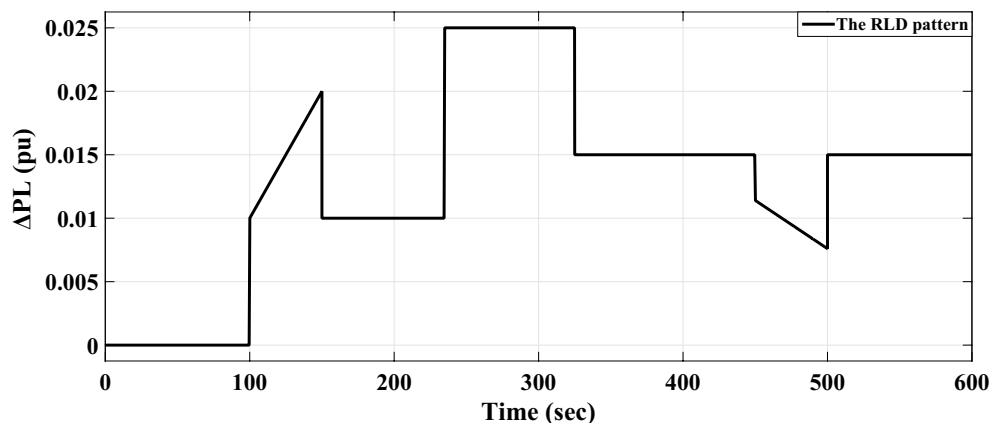


Figure 15. The implemented area-a RLD form.

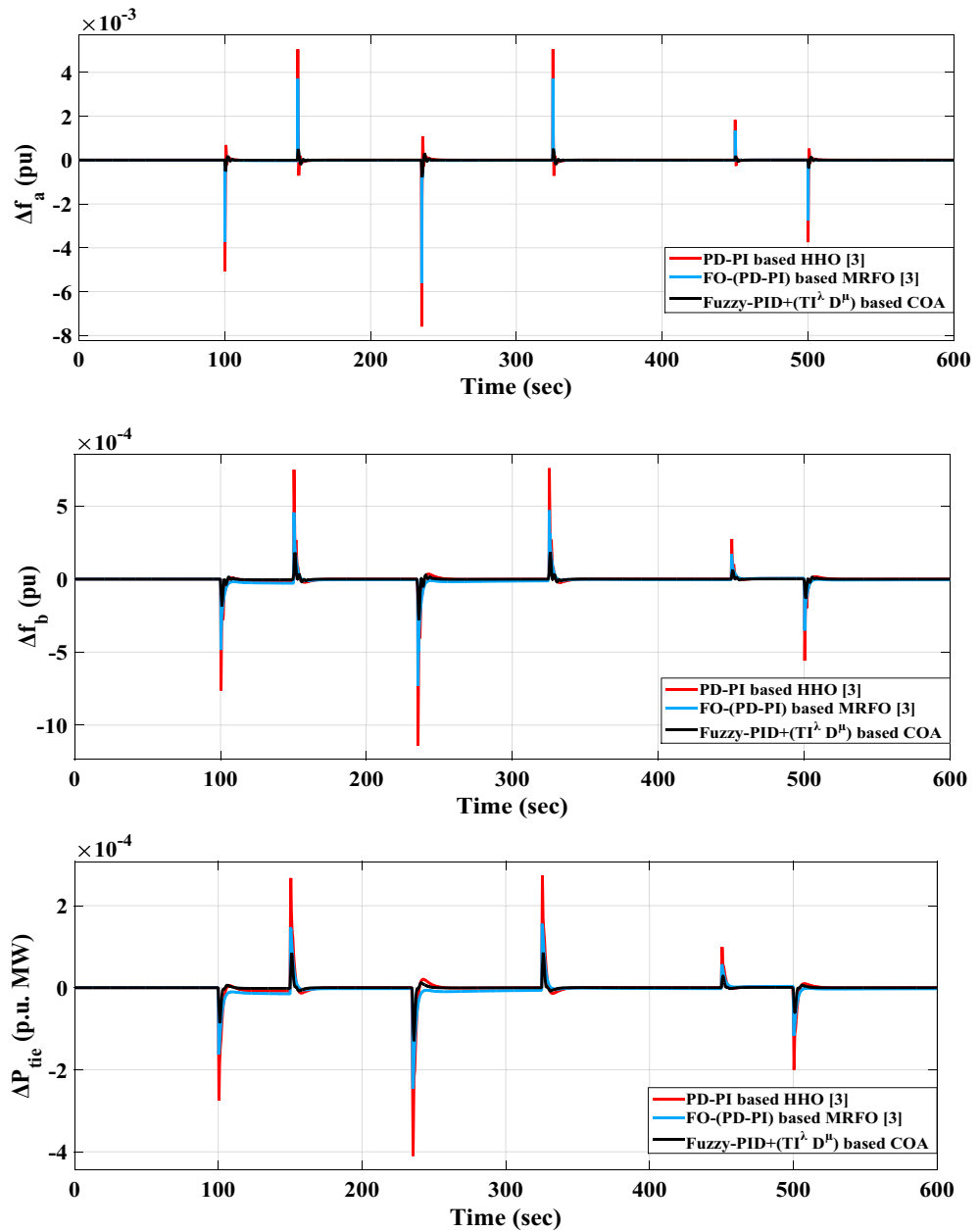


Figure 16. LFC controllers’ dynamic responses to RLD for Case A.3.

Controller structures	Considered dynamic response of (Δf_a)	Considered dynamic response of (Δf_b)	Considered dynamic response of (ΔP_{tie})
PD-PI-optimized via HHO ³	$O_{sh} = 5.06$	$O_{sh} = 0.7597$	$O_{sh} = 0.27321$
	$U_{sh} = -7.591$	$U_{sh} = -1.14$	$U_{sh} = -0.41013$
FO-(PD-PI)-optimized via MRFO ³	$O_{sh} = 3.722$	$O_{sh} = 0.4714$	$O_{sh} = 0.1557$
	$U_{sh} = -5.606$	$U_{sh} = -0.72973$	$U_{sh} = -0.24566$
Fuzzy-PID+($T I^\lambda D^\mu$)-optimized via COA	$O_{sh} = 0.664$	$O_{sh} = 0.20182$	$O_{sh} = 0.08012$
	$U_{sh} = -0.795$	$U_{sh} = -0.3076$	$U_{sh} = -0.1574$

Table 9. Specifications of the analyzed system’s transient response for scenario A.3. All values are multiplied by (10^{-3}).

Controller structures	Δf_a		Δf_b		ΔP_{tie}	
	U_{sh}	O_{sh}	U_{sh}	O_{sh}	U_{sh}	O_{sh}
FO-(PD-PI)-optimized via MRFO ³	26.15	26.44	35.99	37.95	40.10	43.01
Fuzzy-PID+($T^I D^\mu$)-optimized via COA	89.53	86.88	73.02	73.43	61.62	70.67

Table 10. Percentage improvements in O_{sh} and U_{sh} for Case A.3. Optimal percentage values are highlighted in bold format.

where S_i , R_i and H_i refer the specified generation unit's power rating, the factors of both speed regulation and inertia constant respectively related to i^{th} generation units.

The simulation results, using the optimized parameters of the suggested controller listed in Table 13, show improved performance compared to previous studies. The frequencies of the three interconnected areas and the power exchange in various tie lines demonstrate shorter settling times, decreased overshoots, and undershoot. Specifically, the suggested controller outperforms the I controller and FO-(PD-PI) controller used in^{3,54} respectively. Figure 20 displays the distinct SLD profiles experienced by the three interconnected areas. The dynamic responses of the system, presented in Fig. 21, highlight the proposed controller's substantial performance in minimizing excursions and preserving system stability.

Figure 21 depicts that the proposed controller improves the system performance by 96.43% and 94.74% when compared to the I controller and FO-(PD-PI) controller, respectively.

Scenario D: Evaluating the efficacy of the recommended controller utilizing a real-time IEEE-39 bus system, considering high renewables penetration within the system, to assess its effectiveness with the goal to attain dependability and stability.

Similarly, this scenario involves the suggested controller's real-time validation using the IEEE-39 bus system, but with a specific focus on diminishing frequency excursions. The evaluation takes into account the high renewable energy penetrations within the system as depicted in Fig. 19. In this study, ten wind power plants and ten PV power plants have penetrated into areas 1 and 2 of the IEEE-39 bus system via switches (s1) and (s2) respectively. Figure 22 depicts a fair maiden comparison clarifying the superior performance of the proposed controller in attaining the system frequency to a closely predefined value (≈ 50 HZ) over the performance of PID controller tuned by COA. Table 14 presents the obtained optimal PID controller parameters optimized by COA.

Figure 22 shows that the proposed controller strengthens the system performance by 75.19% when compared to the PID controller tuned via COA considering high renewables penetration in the studied system.

Scenario E: Evaluating the performance of the proposed controller under varying CDT conditions before and after the LFC in the IEEE-39 bus system. This evaluation also considers high renewable energy penetrations.

To validate the proposed controller, experiments were conducted on the IEEE-39 bus system. The system was designed to incorporate high penetration levels RESs. In these experiments, different CDT values were introduced before and after the supplementary controllers. When the CDT challenge is executed, Fig. 23 provides a sufficient comparison of the considered system dynamic responses.

The proposed controller demonstrates its capability to effectively handle the perturbations caused by RESs and the challenges posed by CDT. It successfully maintains the frequencies of different areas within predefined values. This highlights the proposed controller's durability in addressing the complexities introduced by RESs and communication delays, ultimately ensuring stable and reliable operation of the system.

Scenario F: Evaluating the proposed strategy's effectiveness by comparing the effectiveness of the IEEE 39 buses system with and without the proposed strategy, considering high renewables penetration.

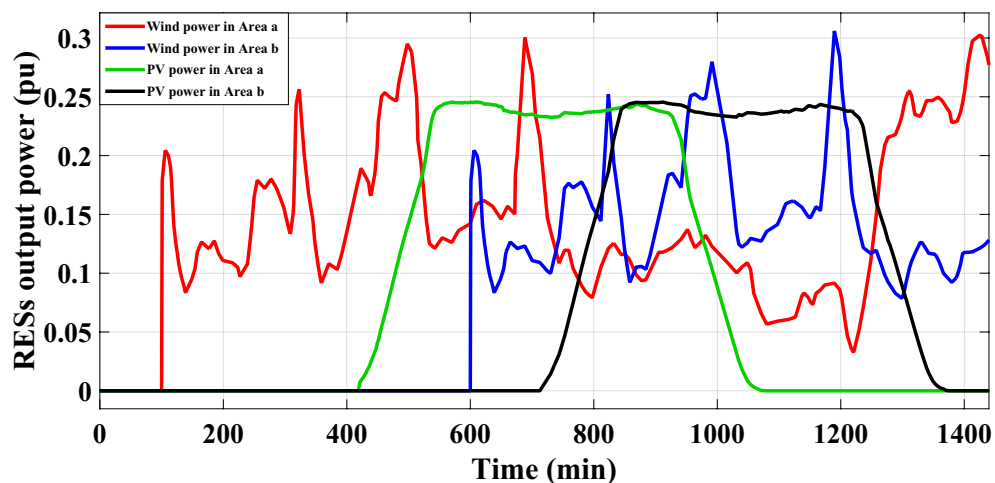


Figure 17. The high renewable energy penetration's generated output power in areas (a) and (b) for Case B.

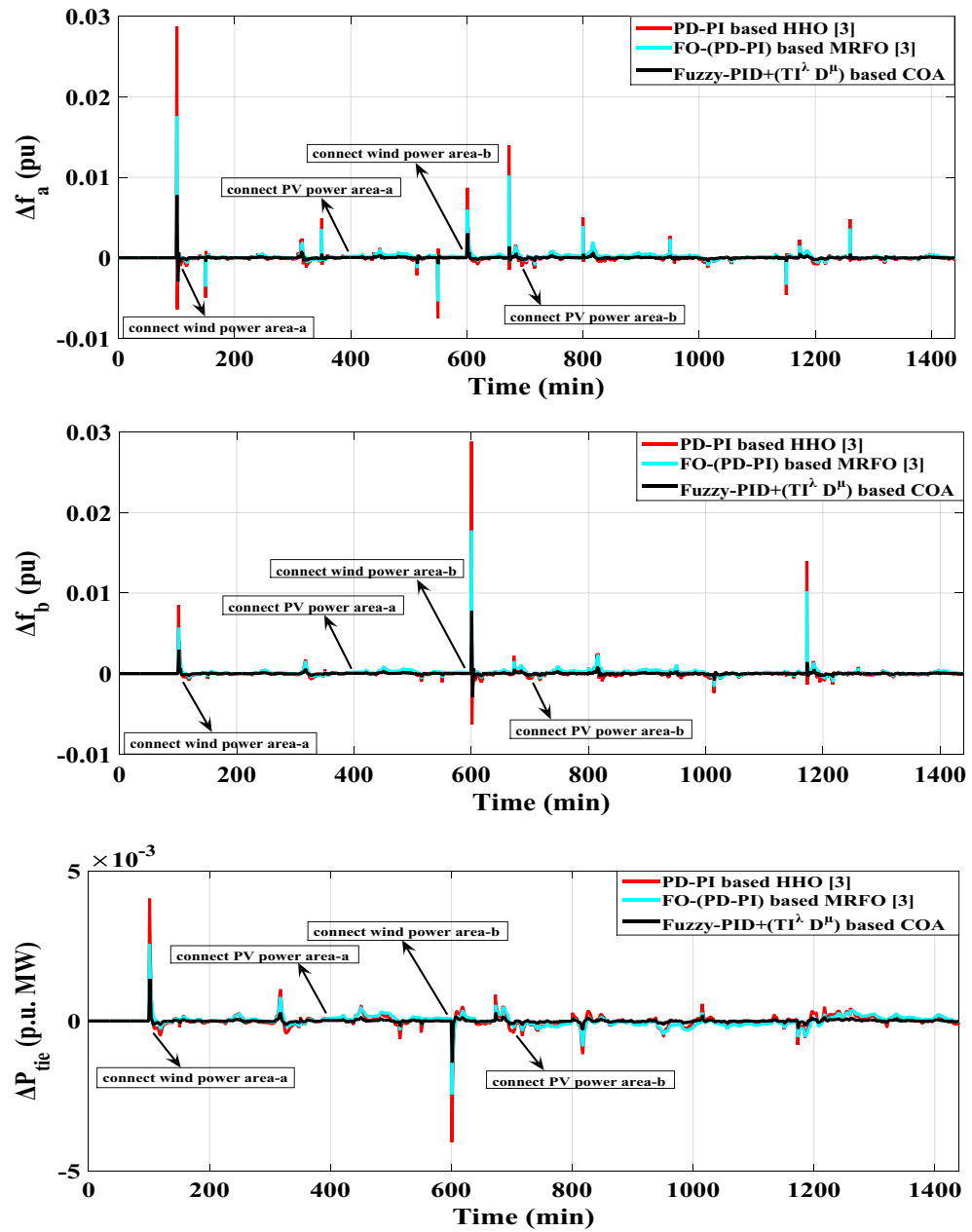


Figure 18. LFC controllers’ dynamic responses to high penetration levels of RESs and RLD pattern for Case B.

Controller structures	Considered dynamic response of (Δf_a)	Considered dynamic response of (Δf_b)	Considered dynamic response of (ΔP_{tie})
PD-PI-optimized via HHO ³	$O_{sh} = 28.742$	$O_{sh} = 28.814$	$O_{sh} = 4.082$
	$U_{sh} = -7.54$	$U_{sh} = -6.32$	$U_{sh} = -4.036$
FO-(PD-PI)-optimized via MRFO ³	$O_{sh} = 17.572$	$O_{sh} = 17.774$	$O_{sh} = 2.559$
	$U_{sh} = -5.395$	$U_{sh} = -1.539$	$U_{sh} = -2.45$
Fuzzy-PID+($T I^\lambda D^\mu$)-optimized via COA	$O_{sh} = 8.115$	$O_{sh} = 8.082$	$O_{sh} = 1.129$
	$U_{sh} = -2.334$	$U_{sh} = -0.7005$	$U_{sh} = -1.167$

Table 11. Specifications of the analyzed system’s transient response for scenario B. All values are multiplied by (10^{-3}).

Controller structures	Δf_a		Δf_b		ΔP_{tie}	
	U_{sh}	O_{sh}	U_{sh}	O_{sh}	U_{sh}	O_{sh}
FO-(PD-PI)-optimized via MRFO ³	28.45	38.86	75.65	38.31	39.3	37.31
Fuzzy-PID+($T^I D^\mu$)-optimized via COA	69.05	71.77	88.92	71.95	71.09	72.34

Table 12. Percentage improvements in O_{sh} and U_{sh} for Case B. Optimal percentage values are highlighted in bold format.

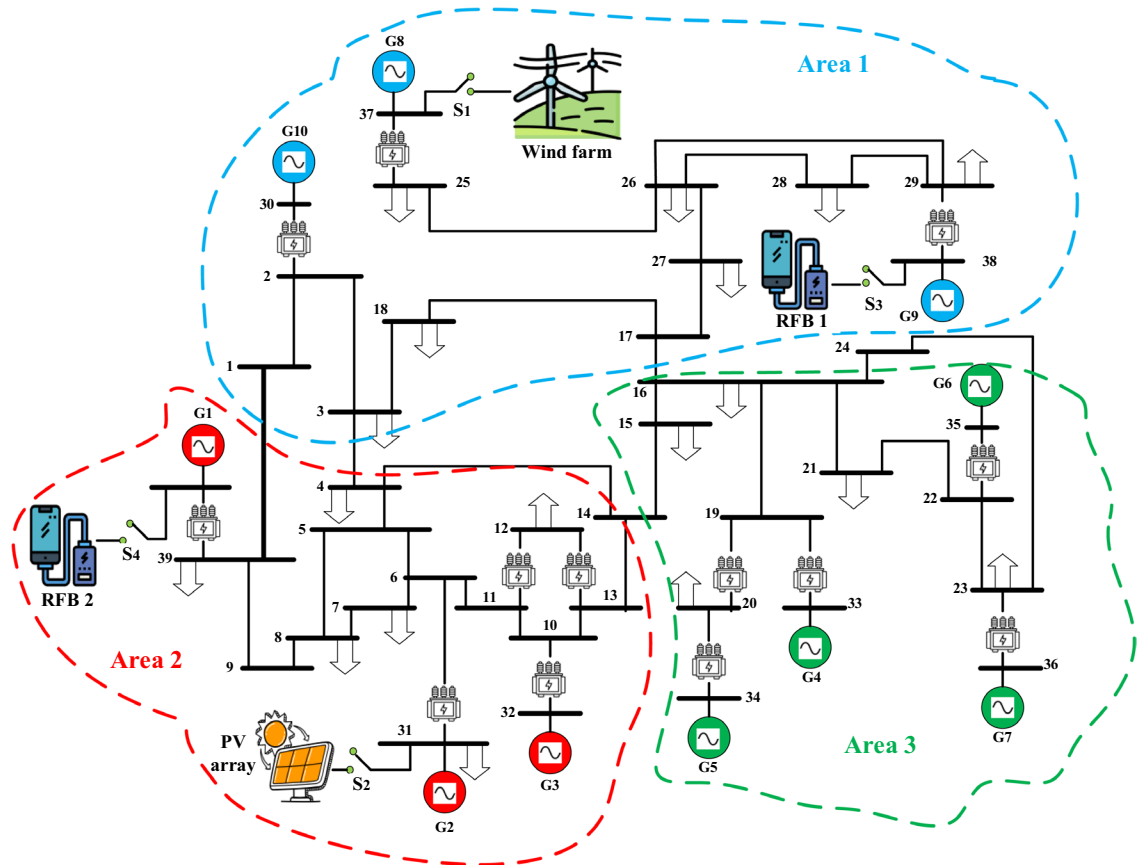


Figure 19. The standard IEEE-39 bus system schematic diagram.

Controller structures	Local area 1	Local area 2	Local area 3
Fuzzy-PID+($T^I D^\mu$)-optimized via COA	$k_1=6.6413, k_2=8.996, k_3=6.1475, k_4=5.4056, k_t=4.8275, k_i=5.3264, k_d=5.98, \lambda=0.8059, \mu=0.4159, n=8.0807$	$k_1=10, k_2=1.1999, k_3=3.7147, k_4=10, k_t=9.6025, k_i=0.8318, k_d=3.6435, \lambda=0.9964, \mu=0.5549, n=1.2751$	$k_1=3.8123, k_2=6.779, k_3=9.8212, k_4=5.2815, k_t=9.7263, k_i=2.434841, k_d=7.913, \lambda=0.5881, \mu=0.1521, n=6.9069$

Table 13. The optimal optimized coefficients of the recommended controller for scenario C.

In this specific scenario, the IEEE-39 bus system performance is examined while considering a significant integration of RESs. Whereas, wind energy is integrated into area 1 at $t = 100$ min, and PV energy is integrated into area 2 at $t = 200$ min. The proposed coordinated strategy involves the incorporation of CRFBs systems in area 1 and area 2. These CRFBs systems work collaboratively by closing switches (s3) and (s4) over different simulation durations. When wind energy penetrates area 1, the CRFBs included in area 1 share their active power with the assessed power system. Additionally, when PV energy penetrates area 2, the CRFBs included in area 2, share their extra active power with the assessed power system. The CRFBs utilize stored energy to enhance LFC and optimize the overall performance of the power system under unusual circumstances. The major objective is to regulate the system frequency, which is prone to considerable fluctuations as a result of the high renewables penetration in both areas. Table 15 illustrates the PID controller variables that were obtained for the proposed

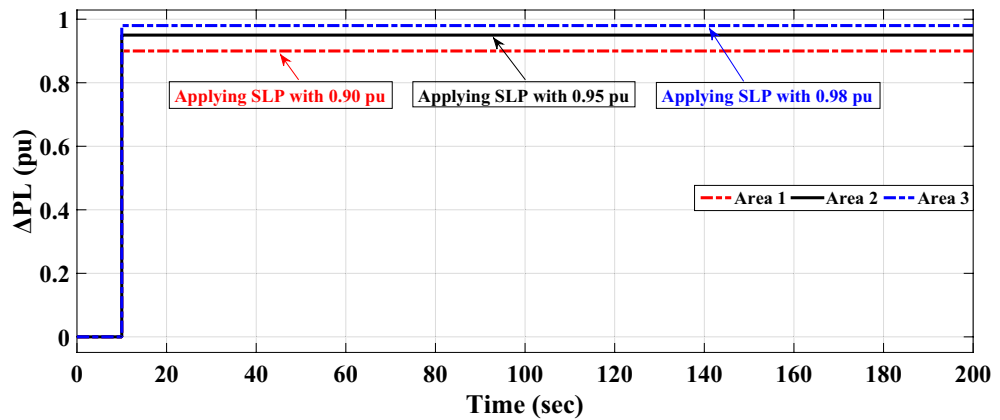


Figure 20. Different load disturbances applied in the three areas.

strategy. Figure 24 depicts the CRFBs systems'-controlled output signal, which denotes the outcome of the active power quantity. Additionally, Fig. 25 compares the total dynamic responses of the entire system in the IEEE-39 bus system with and without the proposed strategy.

Figure 25 indicates that the proposed strategy, which includes the LFC besides CRFBs, demonstrates its capability to successfully handle the perturbations caused by RESs in the studied system. It successfully maintains the frequencies of different areas within predefined values. Whereas, the proposed strategy improves the system performance by 50% as compared to without it.

Scenario G Stability analysis of the proposed (fuzzy-PID) + ($T I^{\lambda} D^{\mu}$) controller

Figure 26 illustrates the bode plot of the loop gains of the analyzed power grid using the proposed (fuzzy-PID) + ($T I^{\lambda} D^{\mu}$) controller. The magnitude of the gain margin plot is observed to be more stable across all frequencies when employing the proposed controller. Additionally, the phase margin shows an infinite value, indicating that the suggested controller is capable of effectively handling system uncertainties.

Conclusion

This study has presented significant findings that contribute to power system stability when transitioning from traditional power stations to renewable energy sources (RESs). Firstly, an effective structure has been presented to ensure stable frequency in the power system during this transition. This structure combines the improved load frequency controller (LFC) and controlled redox flow batteries (CRFBs) to effectively manage frequency fluctuations in considered grid. Furthermore, the controller in LFC depend on (fuzzy-PID) + ($T I^{\lambda} D^{\mu}$) controller. The proposed controller improves the system performance than more on controller such as (PID, FO-PID, PD-PI, and FO-(PD-PI)) controllers. Furthermore, the proposed controller contributes with CRFBs to maintain the system stability during high renewables. The constraints for this proposed scheme have been determined using the crayfish optimization algorithm. LFC controller effectiveness has been validated by comparing its performance to that of other published controllers. Importantly, the proposed strategy demonstrates the ability to maintain system reliability even during periods of high renewable energy penetration. The authors intend to incorporate more ESSs into the system in future research, ensuring its seamless operation throughout the day. Furthermore, as all generation sources will be renewable, the design process took into account the virtual synchronous generator.

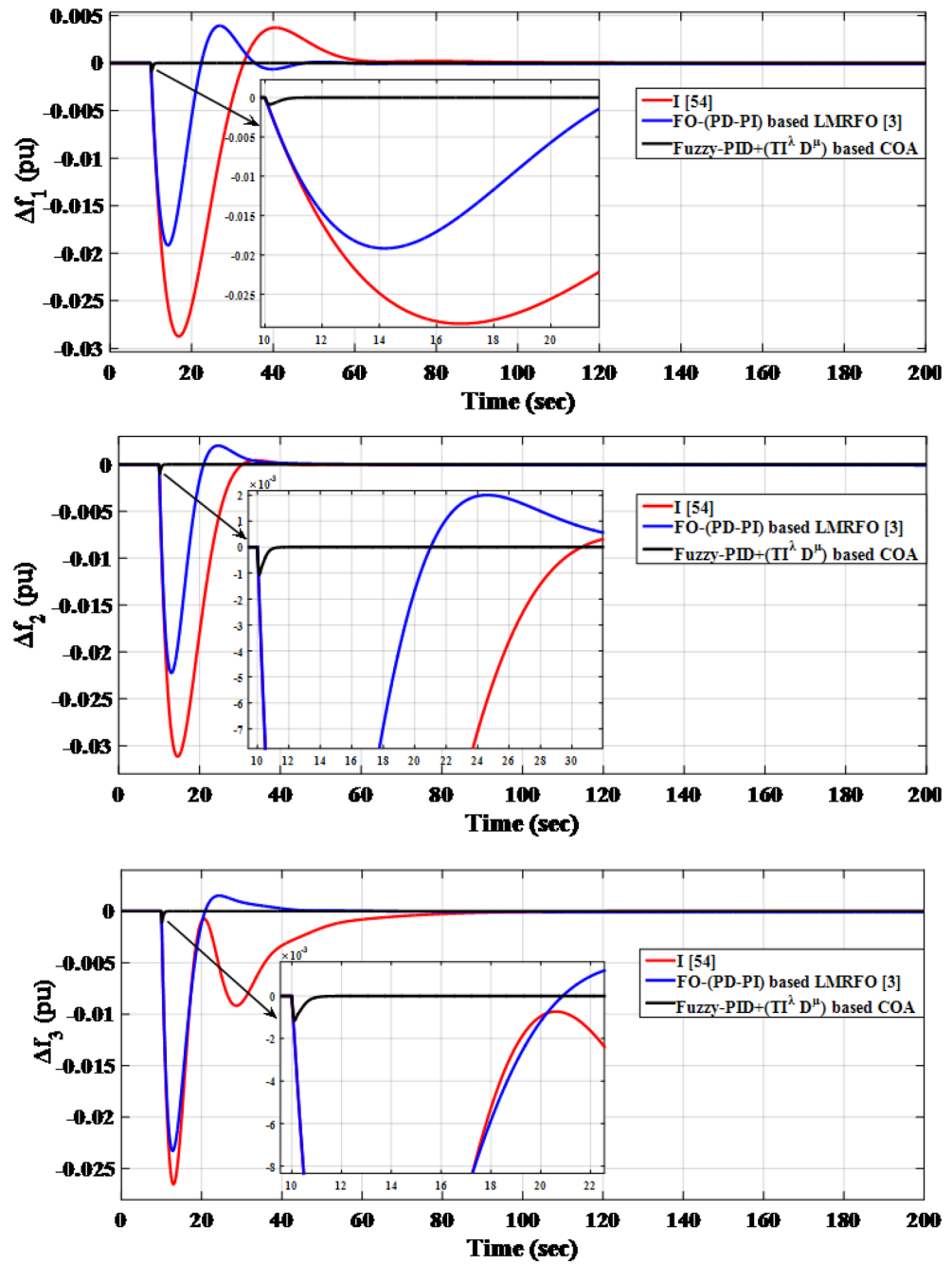


Figure 21. LFC controllers' dynamic responses considering SLD in a standardized IEEE system for Case C.

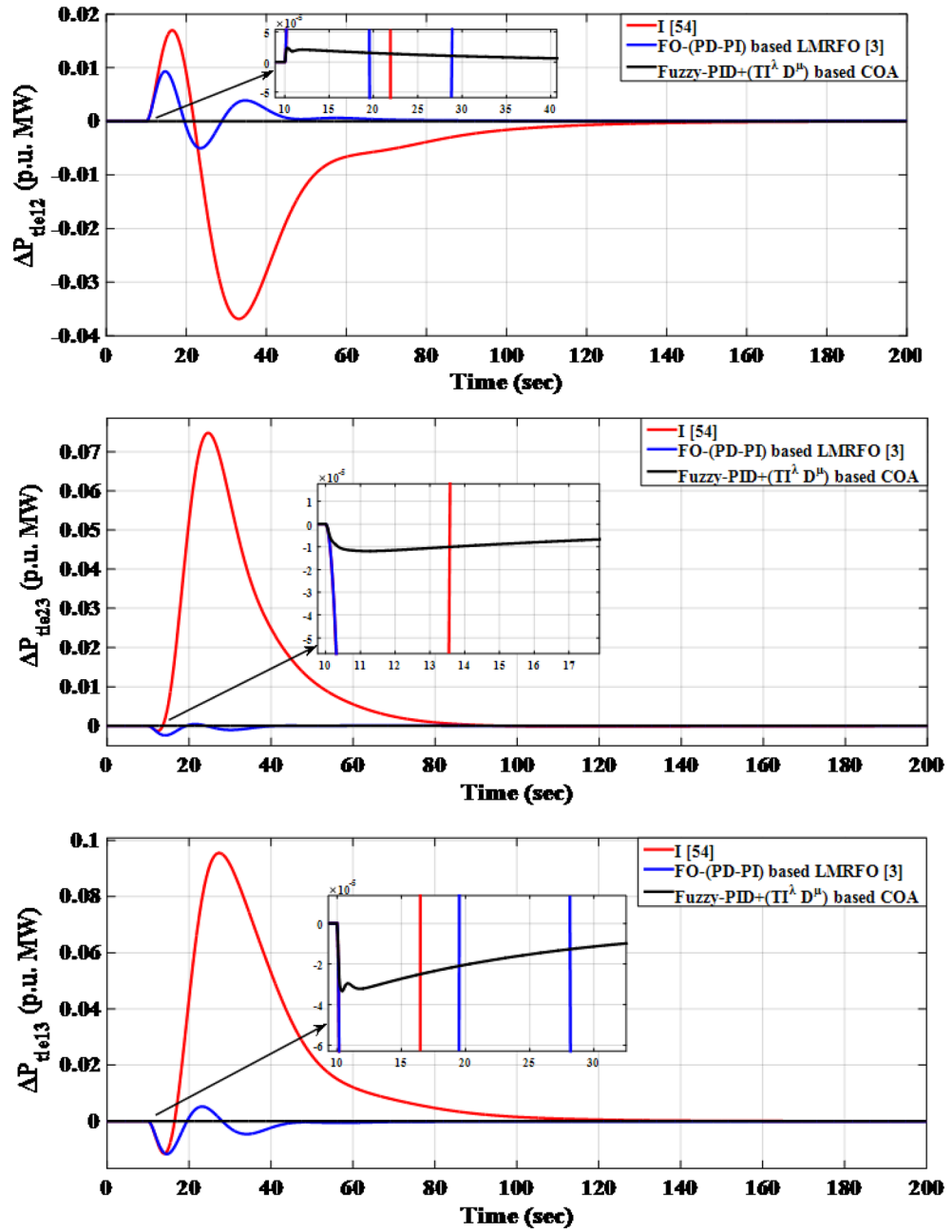


Figure 21. (continued)

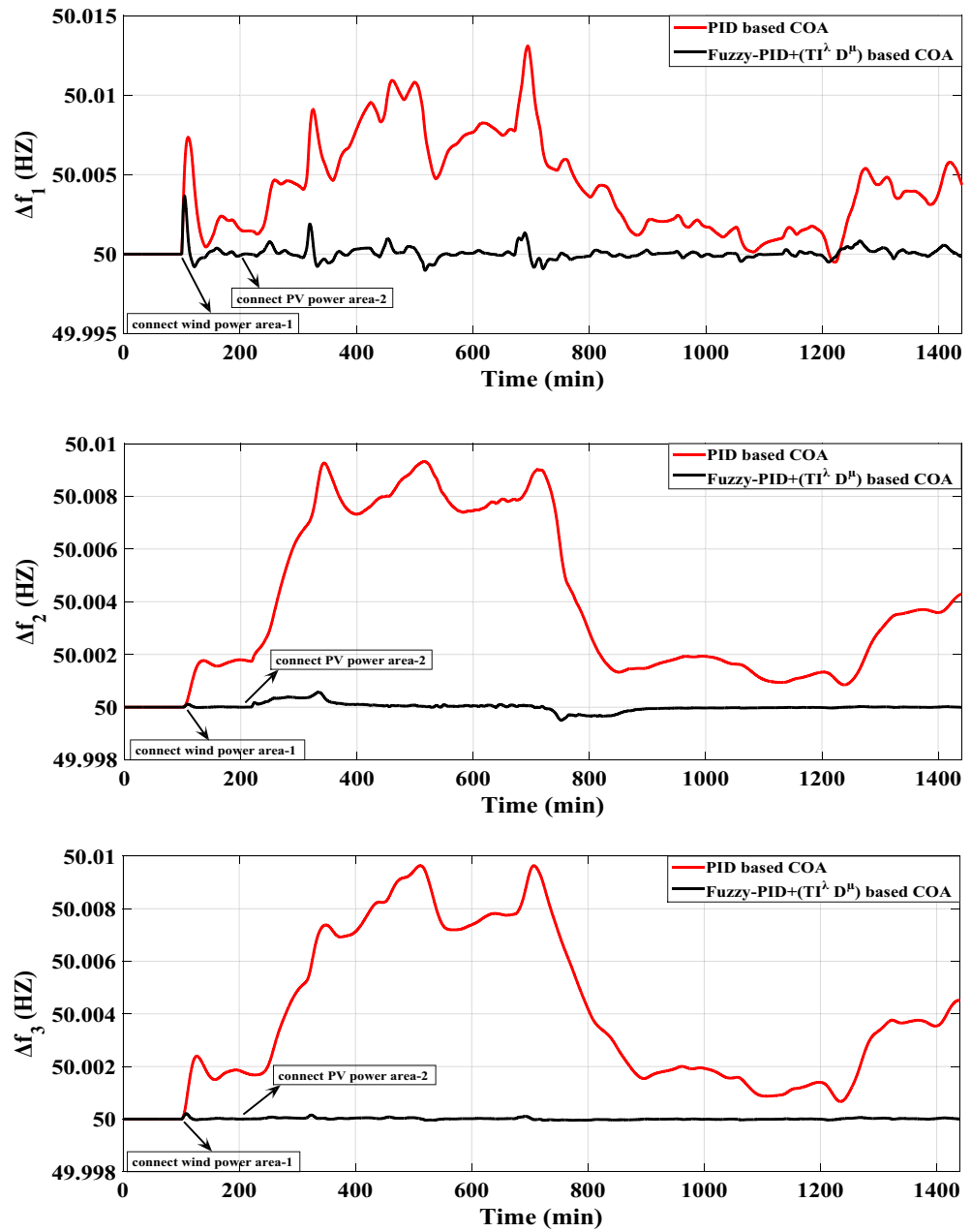


Figure 22. LFC controllers’ considered dynamic responses with high renewables penetration in a standardized IEEE system for Case D.

Controller structures	Local area 1	Local area 2	Local area 3
PID-optimized via COA	$k_p= 9.9789, k_i = 8.6957, k_d = 6.8607$	$k_p= 8.8642, k_i = 2.2517, k_d = 3.9077$	$k_p= 2.2822, k_i = 0.3942, k_d = 2.0487$

Table 14. The Optimum optimized PID controller coefficients for scenario D.

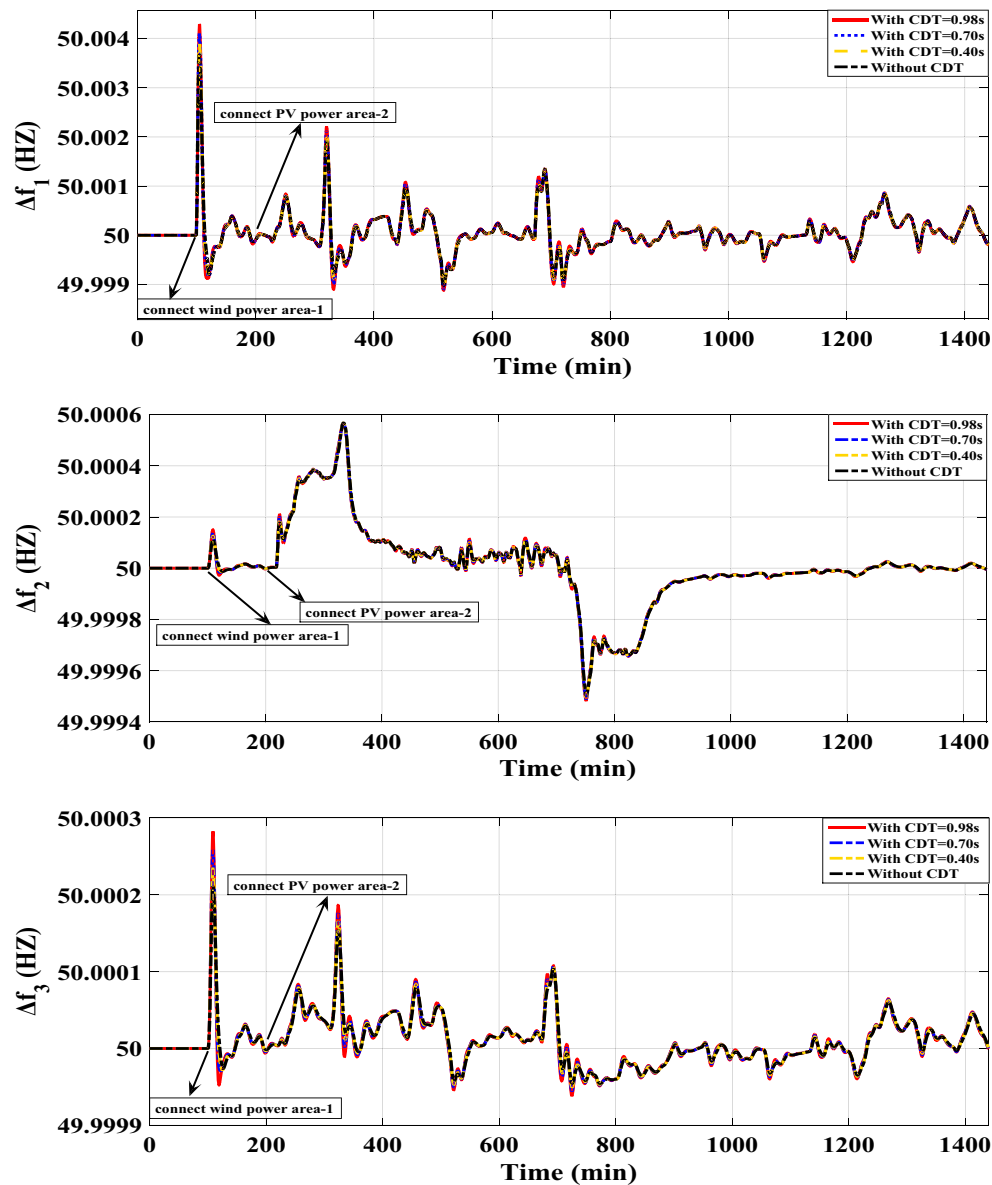


Figure 23. LFC controllers’ considered dynamic responses with high renewables penetration and CDT challenge in a standardized IEEE system for Case E.

Controller Structures	Local area 1	Local area 2
PID-optimized via COA	$k_p = 10, k_i = 10, k_d = 0.0001$	$k_p = 8.4772, k_i = 4.4128, k_d = 5.4788$

Table 15. The optimum values of the PID controller tuned by COA for the proposed strategy.

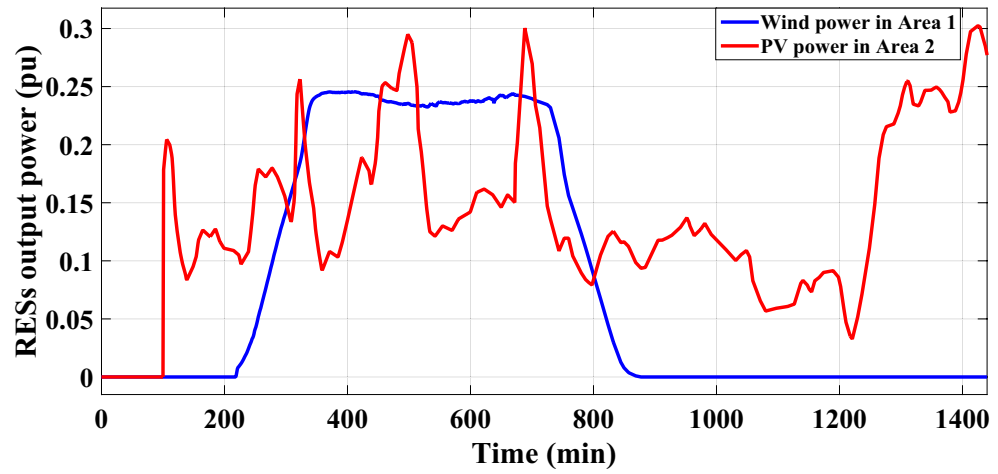


Figure 24. The controllable generated power of the CRFBs systems in both local areas for Case F.

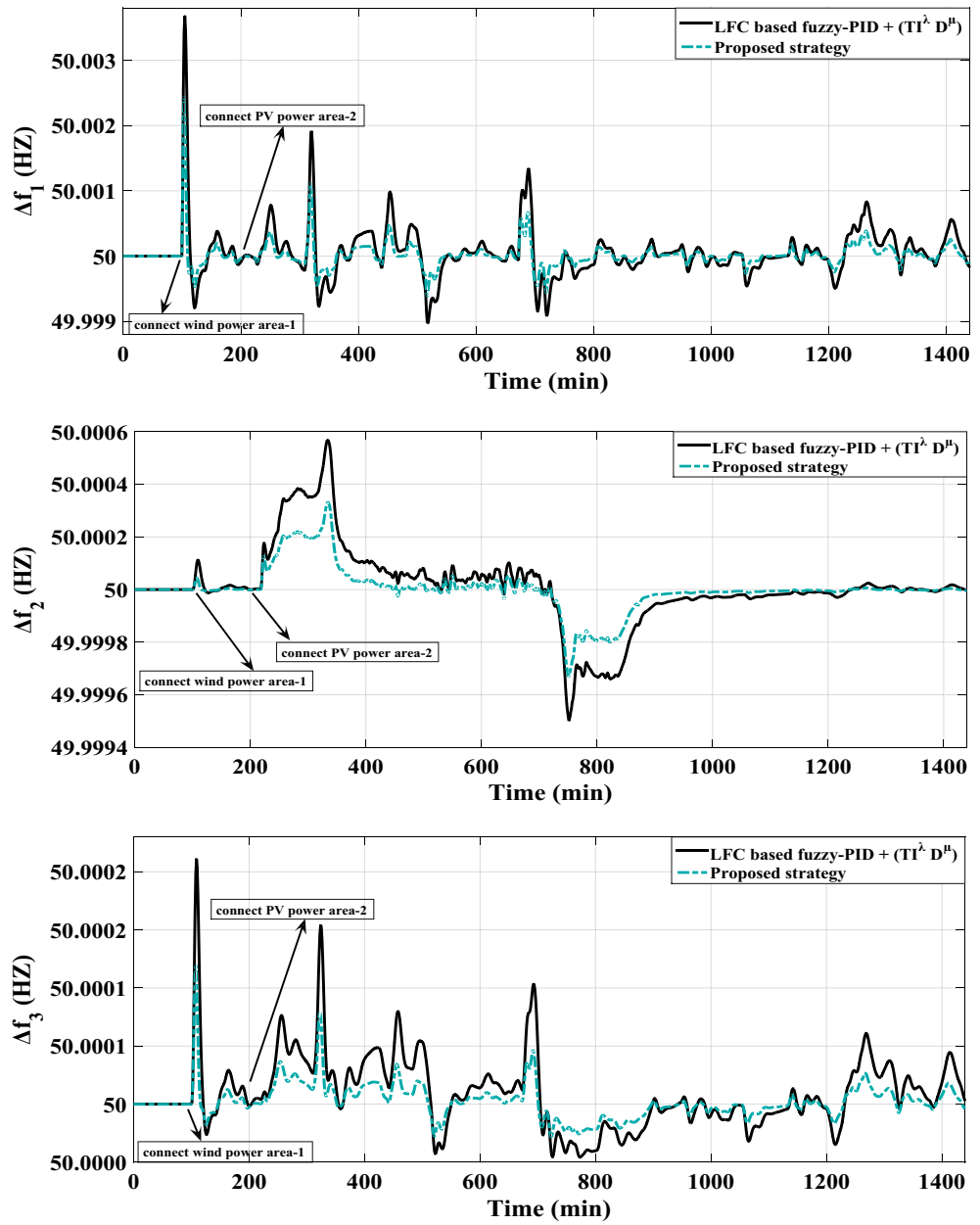


Figure 25. LFC controllers' considered dynamic responses considering a coordinated strategy besides high renewables penetration in the IEEE-39 bus system for Case E.

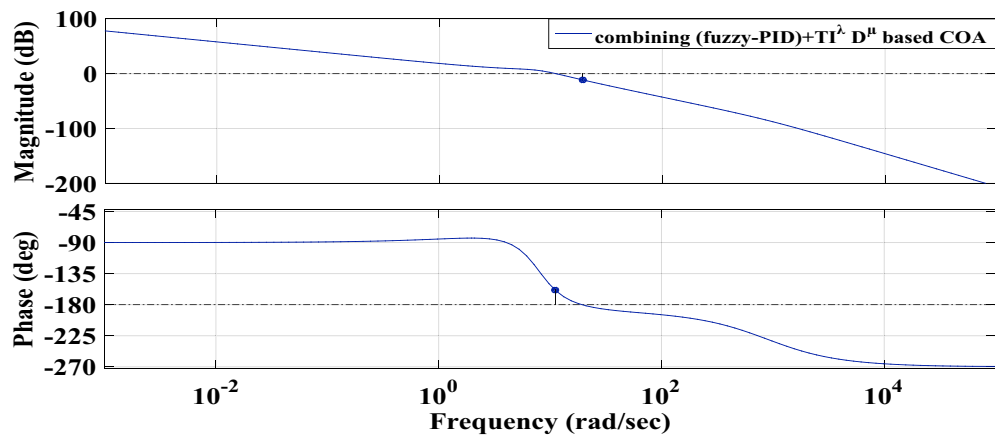


Figure 26. The bode plot of the power grid loop gains with the proposed (fuzzy-PID) + ($T I^2 D^\mu$) controller.

Data availability

All data generated or analysed during this study are included in this published article and its supplementary information file.

Received: 24 December 2023; Accepted: 26 March 2024

Published online: 26 April 2024

References

- Elkasem, Ahmed. H. A., Kamel, S., Khamies, M., Kabalci, E. & Shahinzadeh, H. Frequency Stability Enhancement of Hybrid Multi-area Power Grid Considering High Renewable Energy Penetration Using TID Controller. 2022 4th Global Power, Energy and Communication Conference (GPECOM) <https://doi.org/10.1109/gpecom55404.2022.9815729>. (2022).
- Meng, J. *et al.* Dynamic frequency response from electric vehicles considering travelling behavior in the Great Britain power system. *Appl. Energy* **162**, 966–979 (2016).
- Elkasem, A. H. A., Khamies, M., Hassan, M. H., Nasrat, L. & Kamel, S. Utilizing controlled plug-in electric vehicles to improve hybrid power grid frequency regulation considering high renewable energy penetration. *Int. J. Electr. Power Energy Syst.* **152**, 109251 (2023).
- Ahmed, M., Khamies, M. & Kamel, S. A robust control approach integrating with optimal fuel cells to strengthen the frequency stability of a diverse-sources power system including renewables. *ISA Trans.* **143**, 420–439 (2023).
- Elkasem, A. H. A., Khamies, M., Hassan, M. H., Agwa, A. M. & Kamel, S. Optimal design of TD-TI controller for LFC considering renewables penetration by an improved chaos game optimizer. *Fract. Fract.* **6**, 220 (2022).
- Ahmed, M., Khamies, M., Hassan, M. H., Domínguez-García, J. L. & Kamel, S. A modified controller scheme for frequency stability enhancement of hybrid two-area power grid with renewable energy sources. *IET Renew. Power Gener.* **17**, 1035–1067 (2022).
- Khezri, R., Oshnoei, A., Oshnoei, S., Bevrani, H. & Muyeen, S. M. An intelligent coordinator design for GCSC and AGC in a two-area hybrid power system. *Appl. Soft Comput.* **76**, 491–504 (2019).
- Khamies, M., Kamel, S., Hassan, M. H. & Elnaggar, M. F. A developed frequency control strategy for hybrid two-area power system with renewable energy sources based on an improved social network search algorithm. *Mathematics* **10**, 1584 (2022).
- Ogar, V. N., Hussain, S. & Gamage, K. A. A. Load frequency control using the particle swarm optimisation algorithm and Pid controller for effective monitoring of transmission line. *Energies* **16**, 5748 (2023).
- Zamani, A., Barakati, S. M. & Yousofi-Darmanian, S. Design of a fractional order PID controller using GBMO algorithm for load-frequency control with governor saturation consideration. *ISA Trans.* **64**, 56–66 (2016).
- Debbarma, S., Saikia, L. C. & Sinha, N. Automatic generation control using two degree of freedom fractional order PID controller. *Int. J. Electr. Power Energy Syst.* **58**, 120–129 (2014).
- Arya, Y. & Kumar, N. BFOA-scaled fractional order fuzzy PID controller applied to AGC of multi-area multi-source electric power generating systems. *Swarm Evol. Comput.* **32**, 202–218 (2017).
- Mi, Y. *et al.* The sliding mode load frequency control for hybrid power system based on disturbance observer. *Int. J. Electr. Power Energy Syst.* **74**, 446–452 (2016).
- Sharma, G., Panwar, A., Arya, Y. & Kumawat, M. Integrating layered recurrent ANN with robust control strategy for diverse operating conditions of AGC of the power system. *IET Gener. Trans. Distrib.* **14**, 3886–3895 (2020).
- Oshnoei, A., Kheradmandi, M. & Muyeen, S. M. Robust control scheme for distributed battery energy storage systems in load frequency control. *IEEE Trans. Power Syst.* **35**, 4781–4791 (2020).
- Guha, D., Roy, P. K. & Banerjee, S. Maiden application of SSA-optimised CC-TID controller for load frequency control of power systems. *IET Gener. Trans. Distrib.* **13**, 1110–1120 (2019).
- Abdulnasser, G., Ali, A., Shaaban, M. F. & Mohamed, E. E. M. Stochastic multi-objectives optimal scheduling of energy hubs with responsive demands in smart microgrids. *J. Energy Storage* **55**, 105536 (2022).
- Elkasem, A. H. A., Kamel, S., Hassan, M. H., Khamies, M. & Ahmed, E. M. An eagle strategy arithmetic optimization algorithm for frequency stability enhancement considering high renewable power penetration and time-varying load. *Mathematics* **10**, 854 (2022).
- Mudi, R. K. & Pal, N. R. A self-tuning fuzzy PI controller. *Fuzzy Sets Syst.* **115**, 327–338 (2000).
- Chang, C. S. & Fu, W. Area load frequency control using fuzzy gain scheduling of PI controllers. *Electr. Power Syst. Res.* **42**, 145–152 (1997).
- Yeşil, E., Güzelkaya, M. & Eksin, İ. Self tuning fuzzy PID type load and frequency controller. *Energy Conversat. Manag.* **45**, 377–390 (2004).

22. Ahmadi, S. *et al.* FUZZY aided PID controller is optimized by ga algorithm for load frequency control of multi-source power systems. In *2020 IEEE 18th World Symposium on Applied Machine Intelligence and Informatics (SAMII)* (eds Ahmadi, S. *et al.*) (IEEE, 2020). <https://doi.org/10.1109/sami48414.2020.9108759>.
23. Kwatny, H. G., Kalnitsky, K. C. & Bhatt, A. An optimal tracking approach to load-frequency control. *IEEE Trans. Power Appar. Syst.* **94**, 1635–1643 (1975).
24. Aoki, M. Control of large-scale dynamic systems by aggregation. *IEEE Trans. Automat. Contr.* **13**, 246–253 (1968).
25. Sharma, M., Dhundhara, S., Arya, Y. & Prakash, S. Frequency excursion mitigation strategy using a novel COA optimised fuzzy controller in wind integrated power systems. *IET Renew. Power Gener.* **14**, 4071–4085 (2020).
26. Ali, T., Malik, S. A., Daraz, A., Aslam, S. & Alkhalifah, T. Dandelion optimizer-based combined automatic voltage regulation and load frequency control in a multi-area, multi-source interconnected power system with nonlinearities. *Energies* **15**, 8499 (2022).
27. Ahmed, H. A., E., Kamel, S., Korashy, A. & Jurado, F. Application of Harris Hawks Algorithm for Frequency Response Enhancement of Two-Area Interconnected Power System with DFIG Based Wind Turbine. 2019 21st International Middle East Power Systems Conference (MEPCON) <https://doi.org/10.1109/mepecon47431.2019.9007991>. (2019).
28. Ali, T. *et al.* Load frequency control and automatic voltage regulation in a multi-area interconnected power system using nature-inspired computation-based control methodology. *Sustainability* **14**, 12162 (2022).
29. Hamdy, A., Kamel, S., Nasrat, L. & Jurado, F. Frequency stability of two-area interconnected power system with doubly fed induction generator based wind turbine. *Power Syst.* https://doi.org/10.1007/978-3-030-54275-7_11 (2020).
30. Dhanasekaran, B., Siddhan, S. & Kaliannan, J. Ant colony optimization technique tuned controller for frequency regulation of single area nuclear power generating system. *Microprocess. Microsyst.* **73**, 102953 (2020).
31. Hasanien, H. M. Whale optimisation algorithm for automatic generation control of interconnected modern power systems including renewable energy sources. *IET Gener. Trans. Distrib.* **12**, 607–614 (2017).
32. Paliwal, N., Srivastava, L. & Pandit, M. Application of grey wolf optimization algorithm for load frequency control in multi-source single area power system. *Evol. Intell.* **15**, 563–584 (2020).
33. Kumar, N. K. *et al.* Fuzzy logic-based load frequency control in an island hybrid power system model using artificial bee colony optimization. *Energies* **15**, 2199 (2022).
34. Arya, Y. ICA assisted FTIADN controller for AGC performance enrichment of interconnected reheat thermal power systems. *J. Ambient Intell. Hum. Comput.* **14**, 1919–1935 (2021).
35. Shiva, C. K. *et al.* Load frequency stabilization of stand-alone hybrid distributed generation system using QOHS algorithm. *Int. J. Numer. Model. Electr. Netw. Dev. Fields* **35**, e2998 (2022).
36. Vigya, Shiva, C. K., Vedik, B. & Mukherjee, V. Comparative analysis of PID and fractional order PID controllers in automatic generation control process with coordinated control of TCSC. *Energy Syst.* **14**, 133–170 (2021).
37. Saxena, A., Shiva, C. K., Shankar, R. & Vedik, B. Impacts of wind farms with multi-terminal HVDC system in frequency regulation using quasi-opposition pathfinder algorithm. *Int. J. Syst. Assurance Eng. Manag.* **12**, 1434–1446 (2021).
38. Vigya, *et al.* A novel chaotic chimp sine cosine algorithm part-II: Automatic generation control of complex power system. *Chaos, Solitons Fract.* **173**, 113673 (2023).
39. Mudi, J., Shiva, C. K. & Mukherjee, V. Quasi-oppositional whale optimization optimized load frequency stabilization of hybrid power systems integrated with electric vehicle. *Adv. Theory Simul.* <https://doi.org/10.1002/adts.202100510> (2022).
40. Jia, H., Rao, H., Wen, C. & Mirjalili, S. Crayfish optimization algorithm. *Artif. Intell. Rev.* **56**, 1919–1979 (2023).
41. Pappachen, A. & Fathima, A. P. Load frequency control in deregulated power system integrated with SMES–TCPS combination using ANFIS controller. *Int. J. Electr. Power Energy Syst.* **82**, 519–534 (2016).
42. Pradhan, P. C., Sahu, R. K. & Panda, S. Firefly algorithm optimized fuzzy PID controller for AGC of multi-area multi-source power systems with UPFC and SMES. *Eng. Sci. Technol. Int. J.* **19**, 338–354 (2016).
43. Chidambaram, I. A. & Paramasivam, B. Optimized load-frequency simulation in restructured power system with redox flow batteries and interline power flow controller. *Int. J. Electr. Power Energy Syst.* **50**, 9–24 (2013).
44. Oshnoei, S., Oshnoei, A., Mosallanejad, A. & Haghjoo, F. Novel load frequency control scheme for an interconnected two-area power system including wind turbine generation and redox flow battery. *Int. J. Electr. Power Energy Syst.* **130**, 107033 (2021).
45. Heshmati, M., Noroozian, R., Jalilzadeh, S. & Shayeghi, H. Optimal design of CDM controller to frequency control of a realistic power system equipped with storage devices using grasshopper optimization algorithm. *ISA Trans.* **97**, 202–215 (2020).
46. Peddakapu, K. *et al.* A state-of-the-art review on modern and future developments of AGC/LFC of conventional and renewable energy-based power systems. *Renew. Energy Focus* **43**, 146–171 (2022).
47. Choudhary, R., Rai, J. N. & Arya, Y. Cascade FOPI-FOPTID controller with energy storage devices for AGC performance advancement of electric power systems. *Sustain. Energy Technol. Assess.* **53**, 102671 (2022).
48. Enomoto, K., Sasaki, T., Shigematsu, T. & Deguchi, H. Evaluation study about Redox flow battery response and its modeling. *IEEE Trans. Power Energy* **122**, 554–560 (2002).
49. Selvaraju, R. K. & Somaskandan, G. Impact of energy storage units on load frequency control of deregulated power systems. *Energy* **97**, 214–228 (2016).
50. Gorripotu, T. S., Sahu, R. K. & Panda, S. AGC of a multi-area power system under deregulated environment using redox flow batteries and interline power flow controller. *Eng. Sci. Technol. Int. J.* **18**, 555–578 (2015).
51. Shankar, R., Bhushan, R. & Chatterjee, K. Small-signal stability analysis for two-area interconnected power system with load frequency controller in coordination with FACTS and energy storage device. *Ain Shams Eng. J.* **7**, 603–612 (2016).
52. Parmar, K. P. S., Majhi, S. & Kothari, D. P. Load frequency control of a realistic power system with multi-source power generation. *Int. J. Electr. Power Energy Syst.* **42**(1), 426–433. <https://doi.org/10.1016/j.ijepes.2012.04.040> (2012).
53. Hasanien, H. M. & El-Fergany, A. A. Salp swarm algorithm-based optimal load frequency control of hybrid renewable power systems with communication delay and excitation cross-coupling effect. *Electr. Power Syst. Res.* **176**, 105938 (2019).
54. Pathak, N. & Hu, Z. Hybrid-peak-area-based performance index criteria for AGC of multi-area power systems. *IEEE Trans. Ind. Inform.* **15**, 5792–5802 (2019).

Acknowledgements

The icons used through this paper were developed by Freepik, Amethyst Design, Arkinasi and Smash icons from www.flaticon.com.

Author contributions

AHAE contributed to conceptualization, methodology, software; SK contributed to conceptualization, methodology, software; MK contributed to conceptualization, methodology, software; LN contributed to conceptualization, software, writing—original draft preparation.

Funding

Open access funding provided by The Science, Technology & Innovation Funding Authority (STDF) in cooperation with The Egyptian Knowledge Bank (EKB).

Competing interests

The authors declare no competing interests.

Additional information

Supplementary Information The online version contains supplementary material available at <https://doi.org/10.1038/s41598-024-58189-2>.

Correspondence and requests for materials should be addressed to S.K.

Reprints and permissions information is available at www.nature.com/reprints.

Publisher's note Springer Nature remains neutral with regard to jurisdictional claims in published maps and institutional affiliations.



Open Access This article is licensed under a Creative Commons Attribution 4.0 International License, which permits use, sharing, adaptation, distribution and reproduction in any medium or format, as long as you give appropriate credit to the original author(s) and the source, provide a link to the Creative Commons licence, and indicate if changes were made. The images or other third party material in this article are included in the article's Creative Commons licence, unless indicated otherwise in a credit line to the material. If material is not included in the article's Creative Commons licence and your intended use is not permitted by statutory regulation or exceeds the permitted use, you will need to obtain permission directly from the copyright holder. To view a copy of this licence, visit <http://creativecommons.org/licenses/by/4.0/>.

© The Author(s) 2024